MNRAS 000, 1–15 (—) Preprint 24 August 2018 Compiled using MNRAS LATEX style file v3.0

The GALAH Survey: Verifying abundance trends in the open cluster M67 using non-LTE modelling

Xudong Gao[1,2★], Karin Lind[1,3], Anish M. Amarsi[1], Sven Buder[1,2], Aaron Dotter[4], Thomas Nordlander[5,6], Martin Asplund[5,6], Joss Bland-Hawthorn[7,6,8], Gayandhi M. De Silva[9,6], Valentina D'Orazi[10], Ken C. Freeman[5], Janez Kos[7], Geraint F. Lewis[7], Jane Lin[5,6], Sarah L. Martell[11,6], Katharine. J. Schlesinger[5], Sanjib Sharma[7,6], Jeffrey D. Simpson[11], Daniel B. Zucker[12,9], Tomaž Zwitter[13], Gary Da Costa[5], Borja Anguiano[14], Jonathan Horner[15], Elaina A. Hyde[16], Prajwal R. Kafle[17], David M. Nataf[18], Warren Reid[16,12], Dennis Stello[12,19,6], Yuan-Sen Ting[20,21,22], and the GALAH collaboration

[1]*Max Planck Institute für Astronomy, Königstuhl 17, D-69117 Heidelberg, Germany*
[2]*Fellow of the International Max Planck Research School for Astronomy & Cosmic Physics at the University of Heidelberg, Germany*
[3]*Department of Physics and Astronomy, Uppsala University, Box 516, SE-751 20 Uppsala, Sweden*
[4]*Harvard-Smithsonian Center for Astrophysics, Cambridge, MA 02138, USA*
[5]*Research School of Astronomy & Astrophysics, Mount Stromlo Observatory, Australian National University, ACT 2611, Australia*
[6]*Center of Excellence for Astrophysics in Three Dimensions (ASTRO-3D), Australia*
[7]*Sydney Institute for Astronomy (SIfA), School of Physics, A28, The University of Sydney, NSW, 2006, Australia*
[8]*Miller Professor, Miller Institute, University of California Berkeley, CA 94720, USA*
[9]*Australian Astronomical Observatory, 105 Delhi Rd, North Ryde, NSW 2113, Australia*
[10]*Istituto Nazionale di Astrofisica, Osservatorio Astronomico di Padova, vicolo dell'Osservatorio 5, 35122, Padova, Italy*
[11]*School of Physics, University of New South Wales, Sydney, NSW 2052, Australia*
[12]*Department of Physics and Astronomy, Macquarie University, Sydney, NSW 2109, Australia*
[13]*Faculty of Mathematics and Physics, University of Ljubljana, Jadranska 19, 1000 Ljubljana, Slovenia*
[14]*Department of Astronomy, University of Virginia, P.O. Box 400325 Charlottesville, VA 22904-4325, USA*
[15]*University of Southern Queensland, Toowoomba, Queensland 4350, Australia*
[16]*Western Sydney University, Locked Bag 1797, Penrith South DC, NSW 1797, Australia*
[17]*ICRAR, The University of Western Australia, 35 Stirling Highway, Crawley, WA 6009, Australia*
[18]*Department of Physics and Astronomy, The Johns Hopkins University, Baltimore, MD 21218, USA*
[19]*Stellar Astrophysics Centre, Department of Physics and Astronomy, Aarhus University, DK-8000, Aarhus C, Denmark*
[20]*Institute for Advanced Study, Princeton, NJ 08540, USA*
[21]*Department of Astrophysical Sciences, Princeton University, Princeton, NJ 08544, USA*
[22]*Observatories of the Carnegie Institution of Washington, 813 Santa Barbara Street, Pasadena, CA 91101, USA*

Accepted —. Received —; in original form —

ABSTRACT

Open cluster members are coeval and share the same initial bulk chemical composition. Consequently, differences in surface abundances between members of a cluster that are at different evolutionary stages can be used to study the effects of mixing and internal chemical processing. We carry out an abundance analysis of seven elements (Li, O, Na, Mg, Al, Si, Fe) in 66 stars belonging to the open cluster M67, based on high resolution GALAH spectra, 1D MARCS model atmospheres, and non-local thermodynamic equilibrium (non-LTE) radiative transfer. From the non-LTE analysis, we find a typical star-to-star scatter in the abundance ratios of around 0.05 dex. We find trends in the abundance ratios with effective temperature, indicating systematic differences in the surface abundances between turn-off and giant stars; these trends are more pronounced when LTE is assumed. However, trends with effective temperature remain significant for Al and Si also in non-LTE. Finally, we compare the derived abundances with prediction from stellar evolution models including effects of atomic diffusion. We find overall good agreement for the abundance patterns of dwarfs and subgiant stars, but the abundances of cool giants are lower relative to less evolved stars than predicted by the diffusion models, in particular for Mg.

Key words: radiative transfer — Stars: atmospheres — Stars: abundances — Stars: late-type — Open clusters: individual (M67)

1 INTRODUCTION

Under the assumption that open clusters formed in a single burst of star formation from a chemically homogeneous and well-mixed progenitor cloud (e.g. De Silva et al. 2006, 2007; Pancino et al. 2010; Magrini et al. 2014; Feng & Krumholz 2014) open cluster members are coeval, and share the same initial bulk chemical compositions, differing only in their initial stellar masses. Based on the chemical homogeneity in star clusters, the chemical tagging technique, as proposed by Freeman & Bland-Hawthorn (2002), can be used to reconstruct stellar groups that have dispersed. For example, Kos et al. (2018) have successfully identified two new members of the Pleiades, located far from the cluster centre, with chemical tagging, and recovered seven observed clusters in chemical space by using t-distributed stochastic neighbour embedding (t-SNE). To study Galactic Archaeology by chemical tagging, a large amount of high quality observed data will be provided by massive high resolution spectroscopic surveys such as the GALactic Archaeology with HERMES (GALAH) (De Silva et al. 2015), Gaia-ESO (Gilmore et al. 2012) and APOGEE (Majewski et al. 2017), WEAVE (Dalton et al. 2012), 4MOST (de Jong et al. 2012).

However, recent studies have demonstrated that, in the same open cluster, the surface abundances measured in (unevolved) dwarf stars are apparently offset compared to those measured in (evolved) giant stars (e.g. Villanova et al. 2009; Schuler et al. 2009; Önehag et al. 2014; Martin et al. 2017). These trends with evolutionary stage cannot be explained by the simple stellar evolution model, in which convection is the only internal mixing process.

Atomic diffusion is one possible explanation for these surface abundance trends (Michaud et al. 1984). Atomic diffusion can perturb the surface abundances of dwarfs with shallow convection zones: different chemical species will be underabundant or overabundant to varying degrees in the stellar atmosphere, depending on the competing effects of gravitational settling and radiative acceleration. Furthermore, once the star leaves the turn-off point and starts climbing the red giant branch, the deeper convection zone will restore the original composition in the atmosphere.

Systematic abundance trends with evolutionary stage have also been measured in a number of globular clusters, which can be well described by using atomic diffusion models with extra turbulent mixing below the convection zone (e.g. Korn et al. 2007; Lind et al. 2009b; Nordlander et al. 2012; Gruyters et al. 2014, 2016). However, these globular clusters are old, and only probe the low metallicity regime ($-2.3 < [Fe/H] < -1.5$). They also show anti-correlations in some light elements, which is thought to be produced by intra-cluster pollution by short-lived stars of the first cluster generation (e.g. Prantzos & Charbonnel 2006). In contrast, open clusters probe the metallicity and age range typical of the Galactic disk, and are not expected to have experienced such internal pollution. Thus, the stellar surface compositions of open cluster members should truly reflect the primordial abundances from the protocluster, unless they have been altered by evolutionary effects.

M67 is an ideal target to study such phenomena with a well determined reddening ($E(B-V) = 0.041$) and distance modulus ($\mu = 9.70 - 9.80$; Sarajedini et al. 2009; Yakut et al. 2009), which permits a detailed spectroscopic study of even its main sequence stars. M67 has been widely studied, with the various studies obtaining slightly different results. For example, the averaged metallicities ([Fe/H]) ranges from −0.04 to +0.05 (Hobbs & Thorburn 1991; Tautvaišiene et al. 2000; Yong et al. 2005; Randich et al. 2006; Pasquini et al. 2008; Pace et al. 2008), while determinations of the cluster age vary between 3.5 to 4.8 Gyr (Yadav et al. 2008; Önehag et al. 2011). Considering the uncertainties in the different studies, they are all consistent with the conclusion that chemical composition and age of M67 are similar to those of the Sun. It has even been suggested that this is the original birthplace of the Sun (Önehag et al. 2011), but this has been challenged (Pichardo et al. 2012; Gustafsson et al. 2016).

Previous studies of abundance trends in M67 have been based on small samples (e.g. Tautvaišiene et al. 2000; Yong et al. 2005; Randich et al. 2006; Pace et al. 2008; Pancino et al. 2010). In particular, Önehag et al. (2014) found that heavy element abundances in dwarf stars are reduced by typically 0.05 dex or less, compared to those in sub-giants. Atomic diffusion has already been suggested as the underlying cause for the abundance trends in M67 (Önehag et al. 2014; Bertelli Motta et al. 2017; Souto et al. 2018); we note that, for the mass range of M67 (less than about 2 $M_\odot$), intermediate and heavy elements will not be influenced by nuclear reactions associated with dredge-up (Smiljanic et al. 2016); the light elements Li, Be, and B can be destroyed during the course of the first dredge-up.

However, in order to use the surface abundance trends to make quantitative statements about atomic diffusion processes, the measured surface abundances must be accurate. To date, most abundance analyses have employed the simplifying assumption of local thermodynamic equilibrium (LTE) for the gas in the stellar atmosphere. In reality, conditions in the line-forming regions are such that radiative transitions typically dominate over collisional transitions; the non-thermal radiation field thus drives the gas away from LTE. Thus, to measure surface abundances to better than 0.05 dex, departures from LTE must be taken into account (e.g. Asplund 2005, and references therein). Moreover, the errors arising from the assumption of LTE are systematic, and can therefore result in spurious abundance trends which, if taken to be real, can lead to incorrect conclusions about stellar and Galactic physics. For example, recent studies in open clusters show a remarkable enhancement of Na abundance compared with field stars, however, this Na-enhancement is only an artefact of non-LTE effects, which have been shown by MacLean et al. (2015).

Here we present a detailed non-LTE abundance analysis of lithium, oxygen, sodium, magnesium, aluminium, silicon, and iron, across 66 M67 members. We employ a homogeneous data set drawn from GALAH survey (De Silva et al. 2015), to study how departures from LTE can influence the observed abundance trends in M67. By comparing the trends against recent stellar models that include atomic diffusion, we investigate how departures from LTE influence interpretations about the efficiency of mixing processes in stellar atmospheres.

The rest of paper is structured as follows. In Sect. 2 we describe the observational data used in this study and the sample selection. In Sect. 3 we describe the abundance analysis. In Sect. 4 we present the inferred abundances and consider the abundance trends and the non-LTE effects. In Sect. 5 we discuss these results in relation to others in the literature, as well as to different models of stellar mixing. Our conclusion are presented in Sect. 6.

2 OBSERVATIONAL DATA AND SAMPLE SELECTION

The spectroscopic observations of target stars in M67 were taken from the GALAH survey, whose main science goal is to reveal the formation and evolutionary history of the Milky Way using chemical tagging (Freeman & Bland-Hawthorn 2002). The stars in the GALAH survey were observed with the HERMES spec-

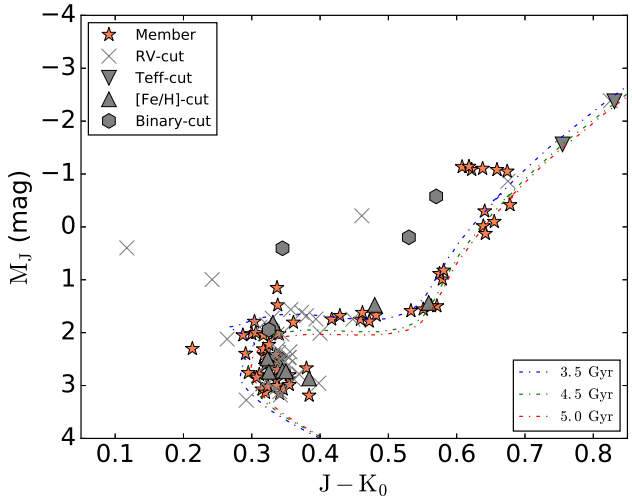

Figure 1. Colour-Magnitude Diagram of the open cluster M67 generated by using the photometric data from 2MASS (Skrutskie et al. 2006) with a distance modulus of 9.70 and reddening E(B − V) = 0.041 mag. The excluded stars are represented by different grey symbols for different selection processes. The cluster members selected and used in this study are marked as filled red star symbols. The spectroscopic binaries found in our final sample are shown as grey hexagon. Solar abundance isochrones corresponding to an age of 3.5 Gyr, 4.5 Gyr and 5.0 Gyr are shown as dot-dashed lines in different colours.

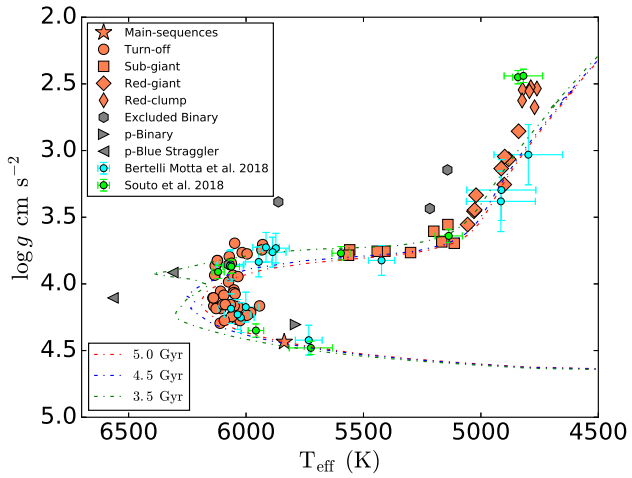

Figure 2. Theoretical isochrones of M67 with solar metallicity and different ages. The sample stars are divided into main-sequence, turn-offs, sub-giants and giants represented by different symbols. The excluded binaries, possible blue stragglers and unresolved binary are also displayed. The effective temperature and gravity of the targeted stars has been offset by 59 K and 0.22 dex, respectively. Results from Bertelli Motta et al. (2018) and Souto et al. (2018) are also shown for comparsion.

trograph (Sheinis et al. 2015) mounted on the Anglo-Australian Telescope (AAT). The spectra provided by HERMES are in fixed format with four noncontiguous wavelength bands, 471.3-490.3 nm (Blue), 563.8-587.3 nm (Green), 647.8-673.7 nm (Red), and 758.5-788.7 nm (IR).

HERMES is designed to operate at two resolution modes for GALAH. During the normal operation, HERMES observes with a resolving powers of $R \sim 28,000$. A higher resolution of $R \sim 42,000$ was used during part of the GALAH pilot survey (Martell et al. 2017). This study is based only on spectra taken in the higher resolution mode (i.e. $R \sim 42,000$). The observations were carried out during the period of 7-14 February 2014. The exposure time ranges from 3600 s to 7200 s. The spectra were reduced using the dedicated GALAH reduction pipeline (Kos et al. 2017), with 2dfdr and IRAF used to perform bias subtraction, flat fielding, wavelength calibration and spectral extraction. The sky background was subtracted from each individual observation. Observed spectra of the same object with different observation dates were stacked for higher signal-to-noise (SNR). All the targets satisfy SNR > 50 in Green, Red and IR arms.

In Fig. 1 we show the colour-magnitude diagram (CMD) for the observed M67 sample (stars with $8.8 < V < 14$). The original candidate list was sourced from the precise optical photometry available from Stetson's database of photometric standard fields [1]. Fig. 1 shows the M_J, $(J - K)_0$ CMD for the stars using the Two Micron All Sky Survey photometry (Skrutskie et al. 2006) with a M67 distance modulus of 9.70 and reddening E(B − V) = 0.041 mag. We determined the radial velocities and spectroscopic stellar parameters as described in Sect. 3.3. To refine the membership selection, we iteratively rejected 2σ outliers in radial velocity. We also excluded two probable members that are cooler than 4500 K, since our approach to determining spectroscopic parameters (based on unblended H and Fe lines) is not reliable at these cool temperatures. Finally, we retained all the stars within 3σ in [Fe/H] as our final sample, thereby rejecting another 8 probable foreground objects of similar radial velocity as the cluster. The abandoned and retained stars are shown in different symbols in Fig. 1.

In Fig. 3 we show histograms of the radial velocity and metallicity distributions of the final sample of stars, together with a Gaussian fit with $< RV >= 34.31\,km\,s^{-1}$ and $\sigma = 0.78\,km\,s^{-1}$, which is consistent with the result from Geller et al. (2015) ($RV = 33.64 \pm 0.96\,km\,s^{-1}$). We also made a cross-match of our targeted stars in SIMBAD (Wenger et al. 2000) by using the coordinates to identify the corresponding objects within a radius of 2 arcsec. We found four stars in our final sample (marked as grey hexagon in Fig. 1) that are listed as spectroscopic binaries in SIMBAD; we excluded these binaries in the sample. Furthermore, by checking the positions of all the left stars in the isochrones (see Fig. 2), we excluded two stars that could be blue stragglers whose temperature are significantly hotter than the other turn-off stars. The coolest dwarf that might well be an unresolved binary has been removed, which lies well above the isochrones in log g. We also see that six stars stand out in Fig. 1 as likely red clump stars. The final stellar sample contains 66 stars with high resolution spectra, including turn-off, sub-giant, red-giant, and red-clump stars, as well as a single solar-like main-sequence star.

3 ABUNDANCE ANALYSIS

The spectra were analysed using a modified version of the GALAH analysis pipeline, which is developed for a full scientific analysis of the GALAH survey and has been applied to determine stellar parameters and abundances in a number of recent studies (e.g. Sharma et al. 2017; Wittenmyer et al. 2017; Duong et al. 2018). The pipeline and the results for the full survey sample are further described and evaluated in GALAH's second data release

[1] http://www.cadc-ccda.hia-iha.nrc-cnrc.gc.ca/en/community/STETSON/st

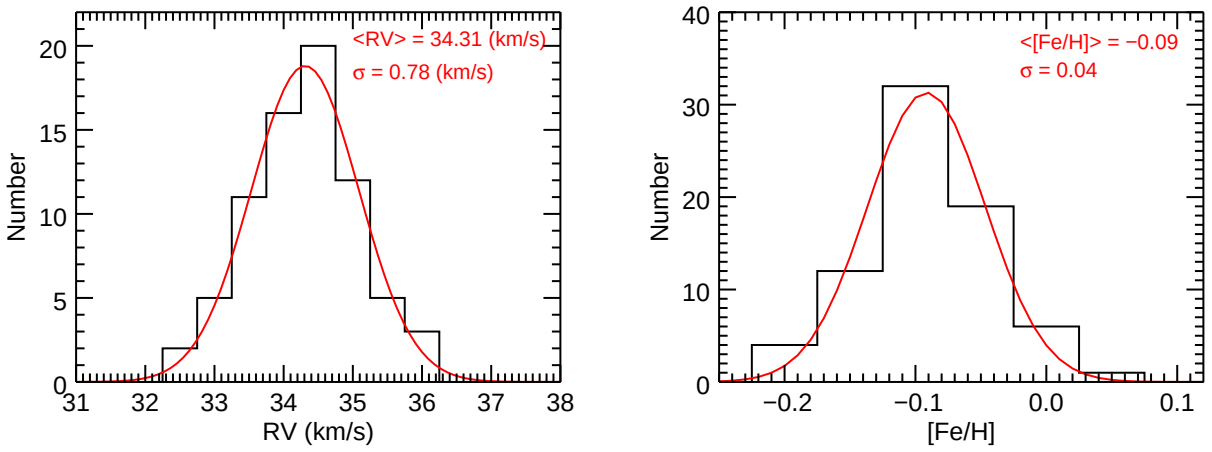

Figure 3. Histogram of the radial velocity and metallicity distributions of the final members selected in M67. The corresponding Gaussian fit to the distributions are also been shown in red lines.

paper (Buder et al. 2018). The input data for this pipeline includes: the reduced observed spectra and corresponding measurement errors (Sect. 2); initial guesses for the stellar atmosphere parameters and radial velocity; reference solar abundances; and a list of atomic and molecular lines. The spectra, which have been radial velocity corrected as described in Kos et al. (2017), were first continuum-normalised using straight lines over 3-60 Å wide segments in all four arms. Wavelength regions contaminated by telluric or sky lines were removed (Buder et al. 2018). The radiative transfer and abundance analysis was carried out using the automated spectrum analysis code Spectroscopy Made Easy (sme; Piskunov & Valenti 2017) We detail aspects of this pipeline in the remainder of this section.

3.1 Atmosphere grids

The spectral line synthesis with sme is based on marcs model atmospheres (Gustafsson et al. 2008) with atmospheric parameters spanning effective temperatures $2500 \leq T_{\rm eff}/{\rm K} \leq 8000$, surface gravities $-0.5 \leq \log_{10}\left(g/{\rm cm\,s^{-2}}\right) \leq 5.0$, and metallicities $-5.0 \leq$ [Fe/H] ≤ 1.0. Spherical models were used for $\log g \leq 3.5$ and plane-parallel models were otherwise used. The standard chemical composition grid was adopted, which uses the solar chemical composition of Grevesse et al. (2007), scaled by [Fe/H], and with an enhancement to α-elements of 0.1 dex for [Fe/H] = −0.25, 0.2 dex for [Fe/H] = −0.5, 0.3 dex for [Fe/H] = −0.75, and 0.4 dex for [Fe/H] ≤ −1.0.

3.2 Non-LTE grids

For non-LTE calculations in sme, instead of solving the non-LTE radiative transfer equations directly, grids of pre-computed departure coefficients $\beta = n_{\rm NLTE}/n_{\rm LTE}$ as functions of optical depth were employed instead, as described in Piskunov & Valenti (2017). When performing the spectral fitting for stellar parameter determinations, as well as the spectral fitting for chemical abundance determinations, the grids of pre-computed departure coefficients (for each stellar model and target abundance) were read in and interpolated based on a given stellar model and non-LTE abundance. Then the corresponding departure coefficients were applied to the corresponding LTE level populations to synthesise the lines.

The non-LTE departure coefficient grids for all the elements were taken from recent non-LTE radiative transfer calculations based on 1D hydrostatic model marcs atmospheres (i.e. consistent with the rest of the analysis). The calculations themselves, and/or the model atoms, were presented in the following studies:

- lithium: Lind et al. (2009a)
- oxygen: Amarsi et al. (2015) (model atom)
- sodium: Lind et al. (2011)
- magnesium: Osorio & Barklem (2016)
- aluminium: Nordlander & Lind (2017)
- silicon: Amarsi & Asplund (2017) (model atom)
- iron: Amarsi et al. (2016b)

We refer the reader to those papers for details on the model atoms; we only provide a brief overview here.

Energy levels and radiative data were taken from various databases, as appropriate or applicable: NIST (Reader et al. 2012), TOPbase (Peach et al. 1988), TIPbase (Bautista 1997), and the Kurucz online database (Kurucz 1995). Inelastic collisional processes, between the species in question and either free electrons or neutral hydrogen atoms, can be a major source of uncertainty in non-LTE analyses (e.g. Barklem 2016a). The oxygen, sodium and magnesium aluminium grids benefit from X+e inelastic collision data based on the R-matrix method (e.g. Burke et al. 1971; Berrington et al. 1974), while the collision data for aluminium is calculated by using the Breit-Pauli distorted wave (Badnell 2011). Both methods are more reliable than commonly used alternatives, such as the van Regemorter recipe (van Regemorter 1962).

Furthermore, more realistic cross-sections for inelastic collisions with neutral hydrogen (X+H) are included in the calculations of all the element grids, which is in turn more reliable than the commonly used Drawin recipe (Steenbock & Holweger 1984; Lambert 1993). To be more specific, for Li, the rate coefficients for inelastic collisions with neutral hydrogen were accounted for (Belyaev & Barklem 2003; Barklem et al. 2003); for O, the rate coefficients were treated by the formula from Drawin (1968) with a correction followed by Lambert (1993); for Na, the rate coefficients were adopted from Barklem et al. (2010); for Mg, the rate coefficients were based on the accurate calculations from Barklem et al. (2012); for Al, the rate coefficients were taken form the computa-

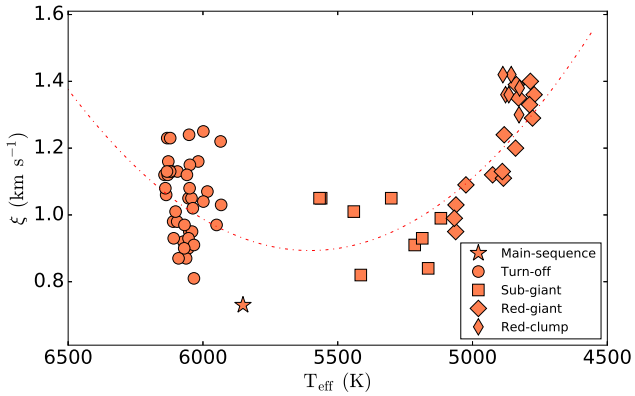

Figure 4. Microturbulence ξ as a function of effective temperature, when treated as a free parameter in stellar parameters calculation. This distribution was fitted by an empirical quadratic polynomial, in order to determine the relation between these two parameters that was subsequently enforced.

tion of Belyaev (2013); for Si, the rate coefficients of low and intermediate levels were used from Belyaev et al. (2014); for Fe I, the rate coefficients were calculated with the asymptotic two-electron method, which was applied to Ca+H in Barklem (2016b). Since the reactions between Fe II and hydrogen are not very prominent, thus for Fe II, the collision excitation with hydrogen was still implemented by the old recipe of Drawin (1968).

3.3 Spectroscopic stellar parameters

To avoid degeneracy issues that result from having too many free model parameters, the analysis separates the determination of the surface elemental abundances from the rest of the stellar parameters, namely the atmospheric parameters $T_{\rm eff}$, $\log g$, [Fe/H], as well as projected rotational velocities $v \sin \iota$, and line-of-sight radial velocity RV. In addition, microturbulence ξ and macroturbulence $v_{\rm mac}$ are standard parameters in 1D atmosphere analysis used to model the impact of convective motions on the spectral lines (e.g. Gray 2005, Chapter 17). In principle, ξ could be set as a free parameter when fitting the spectrum, but we find that this parameter has similar values for similar stars. Additionally, macroturbulence and projected rotation $v \sin \iota$ have a degenerate influence on spectral line broadening and cannot been disentangled, especially for the slowly rotating cool stars. Therefore, in this project we applied fixed values for ξ, which are obtained from an empirical relation as a function of $T_{\rm eff}$ (see Fig. 4), while we treated $v \sin \iota$ as a free parameter with a rotational broadening profile (e.g. Gray 2005, Chapter 18) and set $v_{\rm mac}$ as zero. During this procedure, the synthetic spectra were also convolved with a Gaussian instrumental profile of varying resolution over each arm, which is the dominant source of broadening.

The stellar parameters were determined simultaneously, by fitting (via χ^2 minimisation) the observed profiles of Sc I, Sc II, Ti I, Ti II, Fe I, and Fe II lines that were unblended and that had reliable atomic data, as well as two of the Balmer lines: Hα and Hβ. The benefit of this approach is that, for example, both the temperature sensitive Balmer line wings and the excitation-balance of neutral iron-peak species strongly influence the effective temperature determination; similar statements can be made for the inferred surface gravity and metallicity (Sect. 3.2). In this process, iron was treated in non-LTE (Amarsi et al. 2016b), unless otherwise stated. The non-LTE effects on iron lines are small, for late-type stars of solar-metallicity (e.g. Lind et al. 2012) and we find this choice has only a small influence on the values of the other stellar parameters (the mean differences in $T_{\rm eff}$ and $\log g$ under the assumption of LTE and non-LTE are 3.5 K and 0.01 dex, respectively).

As described in GALAH's second data release paper (Buder et al. 2018), a bias in surface gravity of 0.15dex and a bias in metallicity of 0.1dex is found for purely spectroscopic SME results when compared to results including interferometric, astrometric, and/or asteroseismic constrains. These offsets were applied to all survey targets in Buder et al., in a similar fashion to other large spectroscopic surveys, such as in APOGEE (Holtzman et al. 2015, Sect. 5) and RAVE (Kunder et al. 2017, Sect. 6).

In this study, we chose to use only the Sun as our reference star, because our cluster stars are very close to solar metallicity. By analyzing a high resolution solar spectrum (Sect. 3.5), we find that our analysis pipeline requires positive offsets in $T_{\rm eff}$, $\log g$ and [Fe/H] of 59 K, 0.22 dex and 0.09 dex respectively, to match the reference solar values. We apply these offsets to our spectroscopic parameters before determining chemical abundances.

Since our sample spans a large range in stellar parameters, we could have attempted to design a more sophisticated calibration method involving more reference stars. However, our simple method has the advantage of preserving the relative parameter differences found by spectroscopy and therefore do not strongly influence the derived abundance trends. Our assumption is thus that the internal precision of our spectroscopic method is reliable enough to comment on abundance trends.

As a sanity check, in Fig. 2 we compare our effective temperatures and surface gravities with theoretical cluster isochrones. The three stellar evolutionary tracks and isochrones have been produced using the Padova database (Bressan et al. 2012; Chen et al. 2014; Tang et al. 2014), with solar metallicity ($Z = 0.0142$), but different ages of $t = 3.5$ Gyr, $t = 4.5$ Gyr (close to that of the Sun), and $t = 5.0$ Gyr. The parameters of the stars fall into the reasonable region of the isochrone tracks, without any further calibrations.

3.4 Spectroscopic abundances

In principle, GALAH spectra can allow for up to 30 elements to be determined, but here we only focus on those for which we have non-LTE grids for. Having obtained the optimal stellar parameters (Sect. 3.3), elemental abundances for lithium, oxygen, sodium, magnesium, aluminium, and silicon were then inferred; the abundance of iron was also re-inferred, using only iron lines. The trace element assumption was employed here: i.e. that a small change to the abundances of the particular element being studied has a negligible impact on the background atmosphere and hence the optimal stellar parameters. Thus, the stellar parameters were kept fixed, and the only free parameters were the elemental abundances. The synthesis of the spectral lines incorporated non-LTE departure coefficients (Sect. 3.2).

Unsaturated, unblended lines are preferred as abundance indicators. For partially blended lines in the list, synthetic spectra are fitted in an appropriate selected spectral region that neglects the blended part of the line. Likewise, the abundances were calculated from those lines using χ^2 minimised synthetic fits. All of the lines used in the abundance analysis and their detailed information are presented in Buder et al. (2018). Fig. 5 shows the comparison between observed and best-fit synthetic line profiles of Na, Mg and Si in both LTE and non-LTE for three stars coming from different groups: turn-offs, sub-giants and giants. During these fittings, only abundance is set as a free parameter. Abundance difference between

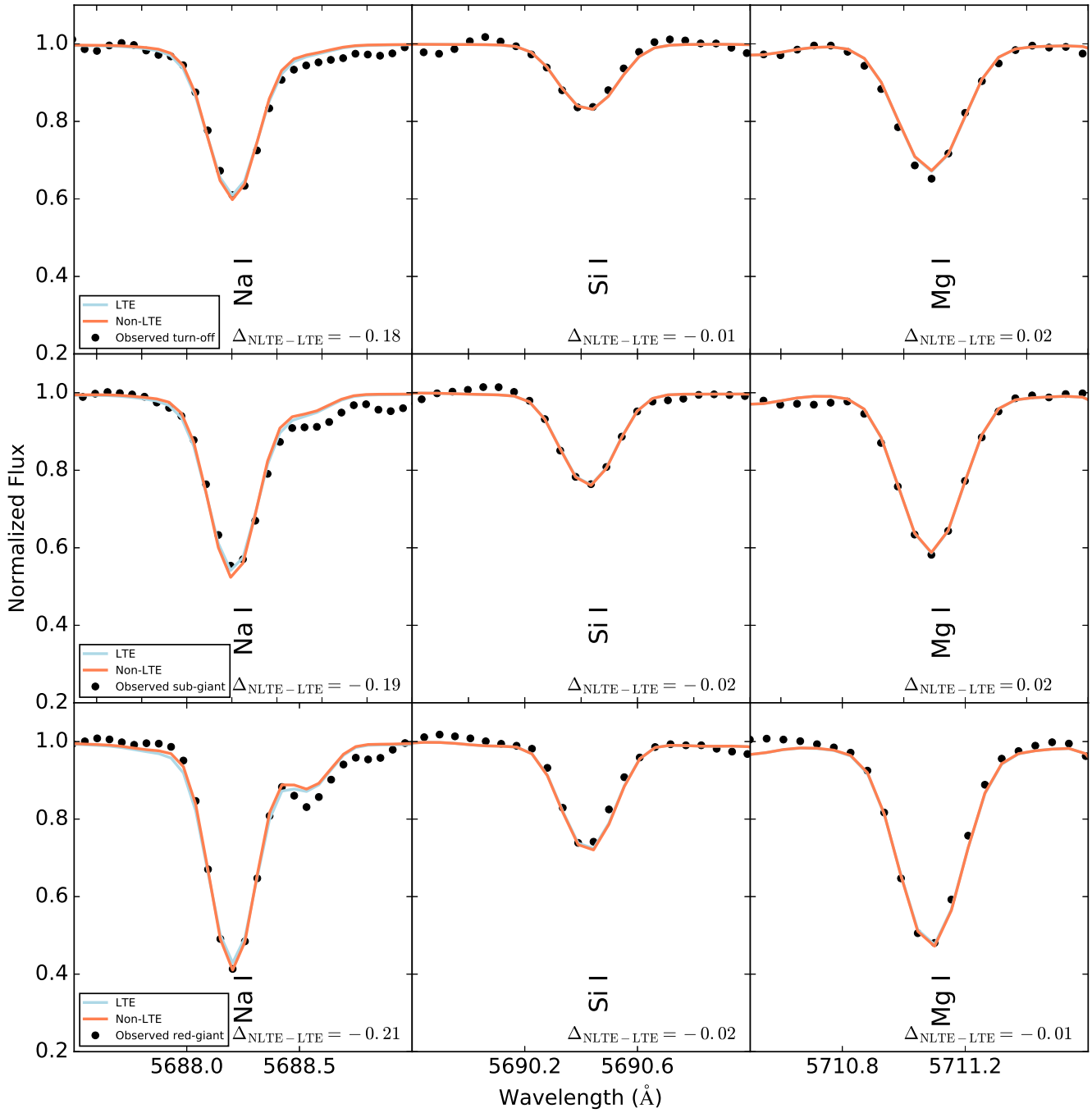

Figure 5. Typical best-fit synthetic LTE and non-LTE line profiles of Na, Mg and Si compared with the observed spectra of three stars in different evolutionary stage; a turn-off, a sub-giant and a giant. Only abundance is set as a free parameters in these fittings. Abundance differences between non-LTE and LTE synthesis are showed in the labels.

non-LTE and LTE synthesis can be substantial, even though all the fits look similar with each other.

3.5 Solar reference

In order to obtain accurate abundance ratios of these late-type stars with respect to the Sun, it is important to determine solar abundances in a consistent manner (e.g. García Pérez et al. 2006). However, we do not have access to a high-quality HERMES solar spectrum observed in the high-resolution mode. Instead, we used the very high-resolution ($R \sim 350,000$) Kitt Peak solar flux atlas of Brault & Neckel (1987). The solar analysis proceeded in the same way as for our M67 targets. The resulting spectroscopic parameters are generally in good agreement with the standard solar values; the spectroscopic $T_{\rm eff}$ is lower by 59 K, $\log g$ is lower by 0.22 dex, and [Fe/H] is lower by 0.09 dex, as we already mentioned in Sect. 3.3. The above offsets were applied to the subsequent solar abundance analysis, as well as to the abundance analysis of all the M67 stars.

Table 1. Comparison of solar abundances with respect to the standard composition of MARCS model atmospheres.

Element	Non-LTE	LTE	Grevesse et al. (2007)
Li	1.00 ± 0.04	0.99 ± 0.04	1.05 ± 0.10
O	8.69 ± 0.09	8.87 ± 0.10	8.66 ± 0.05
Na	6.16 ± 0.03	6.33 ± 0.04	6.17 ± 0.04
Mg	7.62 ± 0.02	7.59 ± 0.02	7.53 ± 0.09
Al	6.43 ± 0.02	6.46 ± 0.02	6.37 ± 0.06
Si	7.46 ± 0.02	7.47 ± 0.02	7.51 ± 0.04
Fe	7.44 ± 0.03	7.42 ± 0.03	7.45 ± 0.05

We list the final inferred solar abundances in Table 1. Our solar abundances are in good agreement with those of Grevesse et al. (2007), the most discrepant elements being magnesium, which is 0.09 dex higher in our non-LTE analysis. Our solar abundances are also very similar to the 1D non-LTE ones presented in Scott et al. (2015a,b); all of our values agree with theirs to within 0.04 dex.

3.6 Error estimation

To estimate the overall precision of atmospheric parameters, we reanalyse all the individual spectra of the 63 stars in our sample that have multiple observations, typically two or three. We compute the maximum difference in atmospheric parameters obtained from individual spectra and adopt the mean values as representative for the entire sample, since we find that these values are fairly independent of S/N and stellar parameters. We finally sum these errors in quadrature with the formal covariance errors returned by SME to obtain the final overall error (effective temperature 40 K, surface gravity 0.14 dex and metallicity 0.07 dex).

The influence of the uncertainties in the atmospheric parameters on our final abundance determinations was assessed by varying each time only one of atmospheric parameters by the amount of their estimated uncertainties. We finally added all the individual errors associated with the three contributors quadratically to obtain the total error in abundances. These internal errors are applied to produce the error bars in the following Fig. 7, Fig. 8, Fig. 9 and Fig. 10. Note that the abundance uncertainties may be underestimated, since we have not taken into account systematic uncertainties.

4 RESULTS

In order to detail the results of our work, we first divide our sample into turn-off stars ($T_{\rm eff;\,DW} > 5800$ K), sub-giant stars (5100 K $< T_{\rm eff;\,SUB} <$ 5800 K), and giant stars ($T_{\rm eff;\,RGB} <$ 5100 K); in Fig. 6 we plot the mean [X/H] abundances for the three groups. In Fig. 7 and Fig. 8 we plot LTE and non-LTE abundances of individual M67 stars as a function of effective temperature. We discuss different aspects of these plots in the remainder of this section.

4.1 Influence of departures from LTE

In Fig. 6 we compare the mean LTE and non-LTE [X/H] abundances for three groups of cluster stars: turn-off stars, sub-giant stars, and giant stars. These were calculated consistently by treating iron in LTE/non-LTE when determining the stellar parameters, and by using our LTE/non-LTE solar reference values. Note that

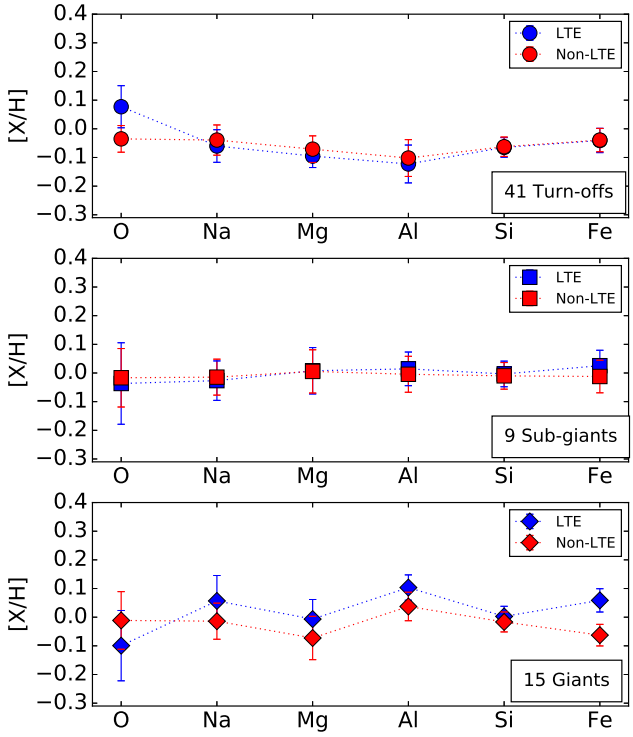

Figure 6. Abundance patterns of turn-off, sub-giant and giant stars in our final sample. LTE/non-LTE [X/H] values were calculated consistently by treating iron in LTE/non-LTE when determining the stellar parameters, and by using our LTE/non-LTE solar reference values. Each symbol represents the mean abundance [X/H] of that group stars, and the error bars correspond to the standard deviation in that group.

part of the absolute NLTE effect on chemical abundances is therefore cancelled and only the differential NLTE effects with respect to the Sun are shown in this plot.

For the turn-off stars, under the assumption of LTE, we find a large overabundance in [O/H] of more than 0.15 dex, compared to the other species. This is caused by the non-LTE effect for O I increasing in magnitude with increasing effective temperature. However, under non-LTE, the abundance ratios [X/H] for all elements are generally consistent with each other at slightly sub-solar values. For the subgiant stars, both LTE and non-LTE abundance results are generally consistent with each other. This group also gives results that are closer to the expected solar abundances (i.e. [X/H] = 0) than the other two groups. For the giant stars, the non-LTE abundances are generally lower than the LTE values, and slightly more consistent with a uniform solar composition.

In Fig. 7 we show LTE and non-LTE abundances as a function of effective temperature for individual member stars of M67. Here, both LTE and non-LTE abundances were calculated by treating iron in non-LTE when determining the stellar parameters, and were put onto a relative ([X/H]) scale using our non-LTE solar reference. This illustrates the departures from LTE in the absolute abundances, as a function of effective temperature. We discuss the departures from LTE for different elements separately, in the following subsections.

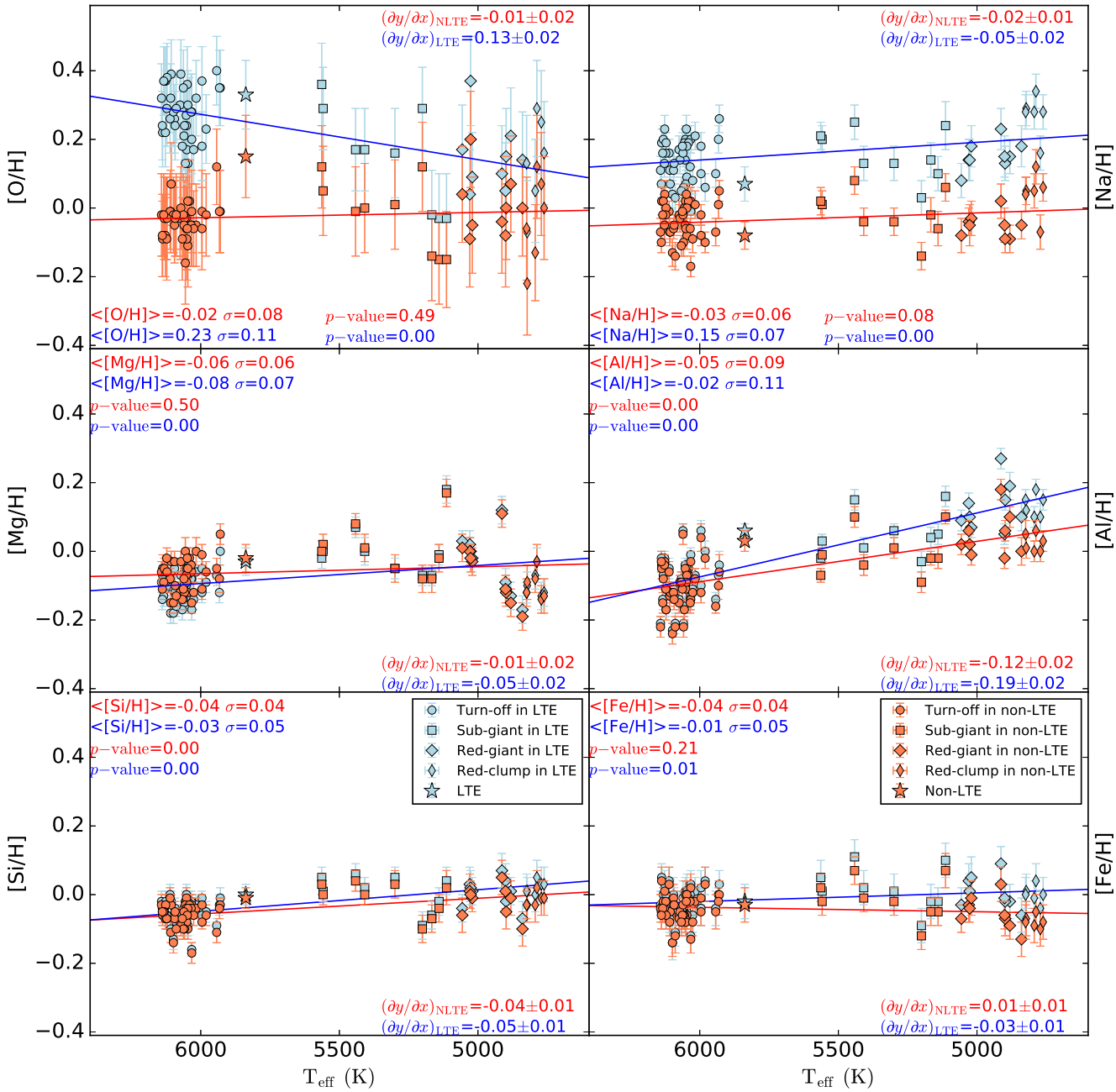

Figure 7. LTE and non-LTE abundances as a function of effective temperature for individual member stars of M67. All LTE and non-LTE abundances shown here were calculated by treating iron in non-LTE when determining the stellar parameters, and were put onto a relative ([X/H]) scale using our non-LTE solar reference. Stars with different evolutionary states are marked using different symbols. The p-values of the trends in LTE and non-LTE are shown in the legends, where a small value (typically p-value $\lesssim 0.05$) is indicative that the trend is significant with respect to the scatter. Beyond that, we also list all the gradients (times by 1000) of weighted linear fitting lines with the standard errors.

4.1.1 Lithium

Lithium abundances were determined from the resonance Li I 670.8 nm doublet. For lithium-poor stars (A(Li) < 2), it was impossible to obtain lithium abundances, because of the very weak line strength. Most stars cooler than 5900 K fall into this category, as they have suffered strong lithium depletion; an added complication in cooler stars is that the doublet is seriously blended with a nearby Fe I line. We found one exception at $T_{\rm eff} \approx 5600$ K, a lithium-rich sub-giant (Sect. 4.2). This star was among those that were rejected as members via the radial velocity criterion. The lithium abundances in the sample are largely insensitive to departures from LTE (see Fig. 8), and the mean Li abundances for non-LTE and LTE calculations are identical and have the same standard deviation: A(Li) = 2.42 ± 0.21.

The scatter around the mean lithium abundances (for those warmer stars in which the doublet could be measured) is large (0.21 dex). This observed spread in our lithium abundance for stars around the solar mass range has also been reported by other M67 studies (Pasquini et al. 2008; Pace et al. 2012). The fundamental

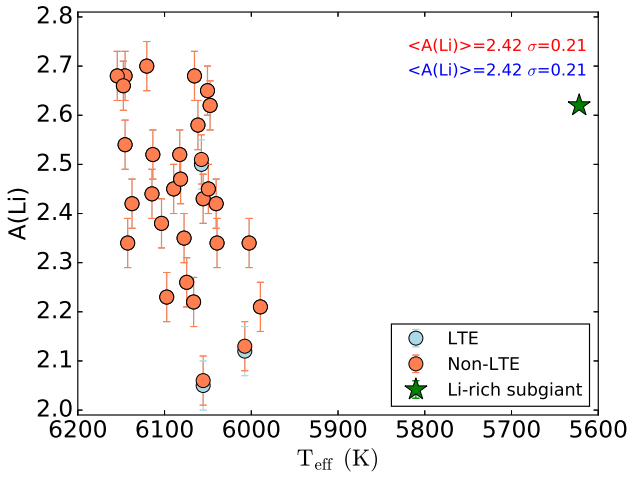

Figure 8. Absolute abundance distributions of lithium as a function of effective temperature. A lithium-rich sub-giant located in a binary system, which we ruled out via our our radial velocity criterion, is marked using an asterisk.

parameters of these turn-off stars (mass, metallicity and age) should be similar; it is possible however that they were born with different initial angular momenta, which is one of the key parameters for rotational mixing, leading to different lithium depletions between these otherwise similar stars (Pinsonneault 2010).

All of the turn-offs in the M67 sample in which we detect lithium have effective temperatures larger than $T_{\rm eff} \approx 5900$ K; in these hot turn-off layers, the combination of overpopulation in the Li ground state and superthermal source function make the non-LTE abundance corrections approximately zero for this line (e.g. Lind et al. 2009a).

4.1.2 *Oxygen*

Oxygen abundances were determined from the O I infra-red triplet, with its three components located at 777.19 nm, 777.42 nm, and 777.54 nm, respectively. The mean non-LTE and LTE abundances of oxygen are $[{\rm O/H}]_{\rm NLTE} = -0.02 \pm 0.08$ and $[{\rm O/H}]_{\rm LTE} = 0.23 \pm 0.11$. The difference between the oxygen abundances using non-LTE and LTE synthesis are large ($\Delta_{\rm non-LTE-LTE} \approx -0.25$ dex). The small line strengths in giant stars and imperfect correction for telluric contamination result in larger star-to-star scatter compared to the other elements studied here, even when LTE is relaxed.

The departures from LTE are mainly due to photon losses in the lines themselves, which leads to an overpopulation of the metastable lower level, and the increased line opacity strengthens the line in non-LTE (e.g. Kiselman 1993; Takeda 2003; Amarsi et al. 2016a). As clearly seen in Fig. 7, the non-LTE abundance corrections are larger in turn-offs (at higher $T_{\rm eff}$) than in giants (at lower $T_{\rm eff}$). This is expected, because the oxygen triplet gets stronger with effective temperature, increasing the photon losses in the lines themselves and hence making the departures from LTE more severe.

4.1.3 *Sodium*

Sodium abundances were determined from the Na I doublet, its components located at 568.26 nm and 568.82 nm. Additionally, the Na I (475.18 nm) line was available for a part of the sample. The mean non-LTE and LTE abundances of sodium are $[{\rm Na/H}]_{\rm NLTE} = -0.03 \pm 0.06$ and $[{\rm Na/H}]_{\rm LTE} = 0.15 \pm 0.07$. Non-LTE effects evidently play an important role in Na line formation and cause a substantial negative correction ($\Delta_{\rm non-LTE-LTE} \approx -0.18$ dex).

The departures from LTE in optical Na I lines are largely driven by photon suction in strong lines, in particular the Na D resonance lines (Na I 588.9 nm and Na I 589.5 nm). A recombination ladder from the Na II reservoir tends to cause overpopulations of lower states and subthermal source functions, resulting in negative abundance corrections that are strongest for saturated lines (e.g. Lind et al. 2011).

4.1.4 *Magnesium*

Magnesium abundances were determined from three lines; Mg I (473.30 nm), the Mg I (571.11 nm), and the Mg I (769.16 nm). The mean non-LTE and LTE abundances of magnesium are $[{\rm Mg/H}]_{\rm NLTE} = -0.06 \pm 0.06$ and $[{\rm Mg/H}]_{\rm LTE} = -0.08 \pm 0.07$. Although the impact of departures from LTE is not very pronounced on the mean abundances, it is interesting to note there is still a clear influence on the abundance trends. This is because the giants tend to have negative abundance corrections, whereas the turn-offs tend to have positive abundance corrections.

The physical non-LTE effect is different in turn-offs and giants. In turn-off stars, the photoionisation rates for the lower Mg I levels are substantial, which can lead to overionisation, resulting in positive non-LTE abundance corrections. In contrast, in giant stars, Mg I lines (especially the Mg I 571.11 nm line) suffer from photon losses, making the abundance corrections negative (e.g. Osorio et al. 2015; Bergemann et al. 2017).

4.1.5 *Aluminum*

Aluminium abundances were determined using the doublet: Al I (669.6 nm) and Al I (669.8 nm). The mean non-LTE and LTE abundances of aluminium are $[{\rm Al/H}]_{\rm NLTE} = -0.05 \pm 0.09$ and $[{\rm Al/H}]_{\rm LTE} = -0.02 \pm 0.11$. The very weak aluminium lines in turn-offs cause a substantial abundance scatter. In addition, the doublet falls in a spectral region where the wavelength calibration of HERMES is of lower quality, which manifests itself in poor synthetic fits to the observed spectral lines. To improve this defect, we set radial velocity as a free parameters when carrying out spectra synthesis of aluminium; this unfortunately further contributes to the abundance scatter.

The non-LTE abundance correction are always negative and become much more severe in giants than the corrections in turn-offs. The negative sign of the corrections is due to photon suction effects, resulting in overpopulations of lower levels and subthermal source functions. These effects are strongest in giants. Towards warmer effective temperatures, the non-LTE effect starts to change: a larger supra-thermal UV radiation field means that a competing overionisation effect becomes more efficient. As such, the non-LTE abundance corrections are much less less severe in turn-offs (Nordlander & Lind 2017) .

4.1.6 *Silicon*

Five silicon lines were used to determine silicon abundances: Si I (566.55 nm); Si I (569.04 nm); Si I (570.11 nm); Si I (579.31 nm),

and Si I (672.18 nm). The mean non-LTE and LTE abundances of silicon are $[Si/H]_{NLTE} = -0.04 \pm 0.04$ and $[Si/H]_{LTE} = -0.03 \pm 0.05$.

The non-LTE abundance corrections for Si lines are not very pronounced, however they are always negative in this sample. Generally, photon losses in the Si I lines drives overpopulation for the lower levels and underpopulation for higher levels, which strengthen the lines in non-LTE.

4.1.7 Iron

Iron abundances were determined from a selection of Fe I and Fe II lines, that are listed in Buder et al. (2018). The mean non-LTE and LTE abundances of iron are $[Fe/H]_{NLTE} = -0.04 \pm 0.04$ and $[Fe/H]_{LTE} = -0.01 \pm 0.05$. Non-LTE effects cause a small negative correction ($\Delta_{non-LTE-LTE} \approx -0.03$ dex).

Since Fe II lines are almost immune to non-LTE effects in late-type stars (at least, in 1D hydrostatic model atmospheres such as those used in this work – in 3D hydrodynamic model atmospheres this is not always the case; e.g. Amarsi et al. 2016b, Table 3), the main contribution to the difference between the mean abundances under the assumption of LTE and non-LTE comes from the Fe I lines. The traditional non-LTE effect for Fe I lines is overionisation; at solar-metallicity, however, this effect is relatively small, and photon losses in the Fe I lines as well as a general photon-suction effect are more important. We therefore see slightly negative abundance corrections. The effects are more severe in giants, where these intermediate-excitation Fe I lines are stronger.

4.2 Lithium-rich sub-giant

Among the full sample of stars observed in the M67 field, we discovered a sub-giant star (S95) with a very high lithium abundance A(Li) = 2.6 (see Fig. 8). However, because of its radial velocity, RV = 38.5 km s^{-1}, which is high compared to the cluster mean (see Fig. 3), we regard this star as a potential non-member and have excluded it from the discussion of cluster abundance trends. No other sub-giant star in the sample has such a high lithium abundance, and severe lithium depletion is expected at this evolutionary stage after leaving the main sequence turn-off (Balachandran 1995; Pace et al. 2012). By checking the position and magnitude information, this star has been confirmed as a spectroscopic binary in the SIMBAD.

Canto Martins et al. (2006) also reported a lithium-rich sub-giant star S1242 with (A(Li) = 2.7). S1242 has been verified as a member of a large eccentricity binary system in M67, with a faint low-mass dwarf companion providing negligible contribution to the luminosity (Sanders 1977; Mathieu et al. 1990). Canto Martins et al. (2006) proposed that high chromospheric activity and unusually high rotational velocity of S1242 may be induced by tidal interaction, which could help the star conserve its lithium abundance from the turn-off stage. Interestingly, Önehag et al. (2014) also found a lithium-rich sub-giant star S1320 with A(Li) = 2.3. This sub-giant has been included in their membership, since they did not find any evidence that this star has been contaminated by a companion. It is worth to follow up these stars, as the identification of these stars should prove useful for providing insight into the processes in binaries that can affect the surface abundances.

4.3 Abundance trends

As illustrated in Fig. 7, we have found abundance trends with effective temperature for some elements. The trends are more pronounced when LTE is assumed; furthermore, the scatter around the mean for oxygen becomes more pronounced when LTE is assumed. Even under the assumption of non-LTE, however, there still exist some systematic abundance differences between turn-offs, sub-giants and giants, as can be seen in Fig. 7.

To determine if there is a significant correlation between element abundance and effective temperature, we calculate p-values in the linear regression analysis by assuming there is no correlation between these two parameters in the null hypothesis. The p-values of the trends are shown in the legends of Fig. 7, where a small value (typically p-value $\lesssim 0.05$) is indicative that the trend is significant with respect to the scatter. We can thus say that, under the assumption of LTE, the trends in surface abundance against effective temperature are significant with respect to the scatter, for all of the species shown in Fig. 7. In contrast, under the assumption of non-LTE, the trends for oxygen, sodium, magnesium and iron are not significant with respect to the scatter, while for aluminium and silicon the trends remain significant. We further note an obvious deviation from the linear trend in the behaviour of Mg abundance with effective temperature; subgiants appear overabundant with respect to the linear trend and red giants underabundant.

In summary, non-LTE analysis tends to flatten the trends with effective temperature seen in LTE, which reduces the scatter in mean abundance for all the elements, when the full sample is considered. The remaining residual trends may reflect other systematic errors still present in the analysis or be intrinsic to the cluster. We shall consider this in more detail in Sect. 5.

5 DISCUSSION

5.1 Comparison with atomic diffusion models

Atomic diffusion is a continuous process whose influence immediately below the outer convection zone causes surface abundance variations during the main-sequence phase of a star. At the turn-off point, where the convective envelope is the thinnest, the settling of elements reaches a maximum. As the star evolves along the sub-giant branch and red giant branch, the surface abundances begin to recover gradually to the initial value due to the enlarged surface convection zone, except for those light elements that are affected by nuclear processing.

The metals in our Sun are thought to be underabundant relative to the initial bulk composition, by about 0.04 dex (e.g. Asplund et al. 2009). Turcotte et al. (1998) demonstrated that the diffusive process is dominant at the end of the main-sequence phases of solar-type stars, thus the turn-off stars in M67 with comparable age to the Sun may show even larger effects of atomic diffusion. Larger effects are also expected in warm metal-poor stars, because of their older ages and thinner surface convection zones (Michaud et al. 1984).

Our sample includes stars in different evolutionary states, including main-sequence, turn-off, sub-giant, red-giant and red-clump stars. It is therefore of interest to compare our results with those predicted by stellar evolutionary models that include atomic diffusion. We adopted the surface abundances that were calculated in Dotter et al. (2017) with solar metallicity, initial masses ranging from 0.5M$_\odot$ to 1.5M$_\odot$ and ages of t = 4.0 Gyr, t = 4.5 Gyr and t = 5.0 Gyr, respectively. The stellar evolutionary models

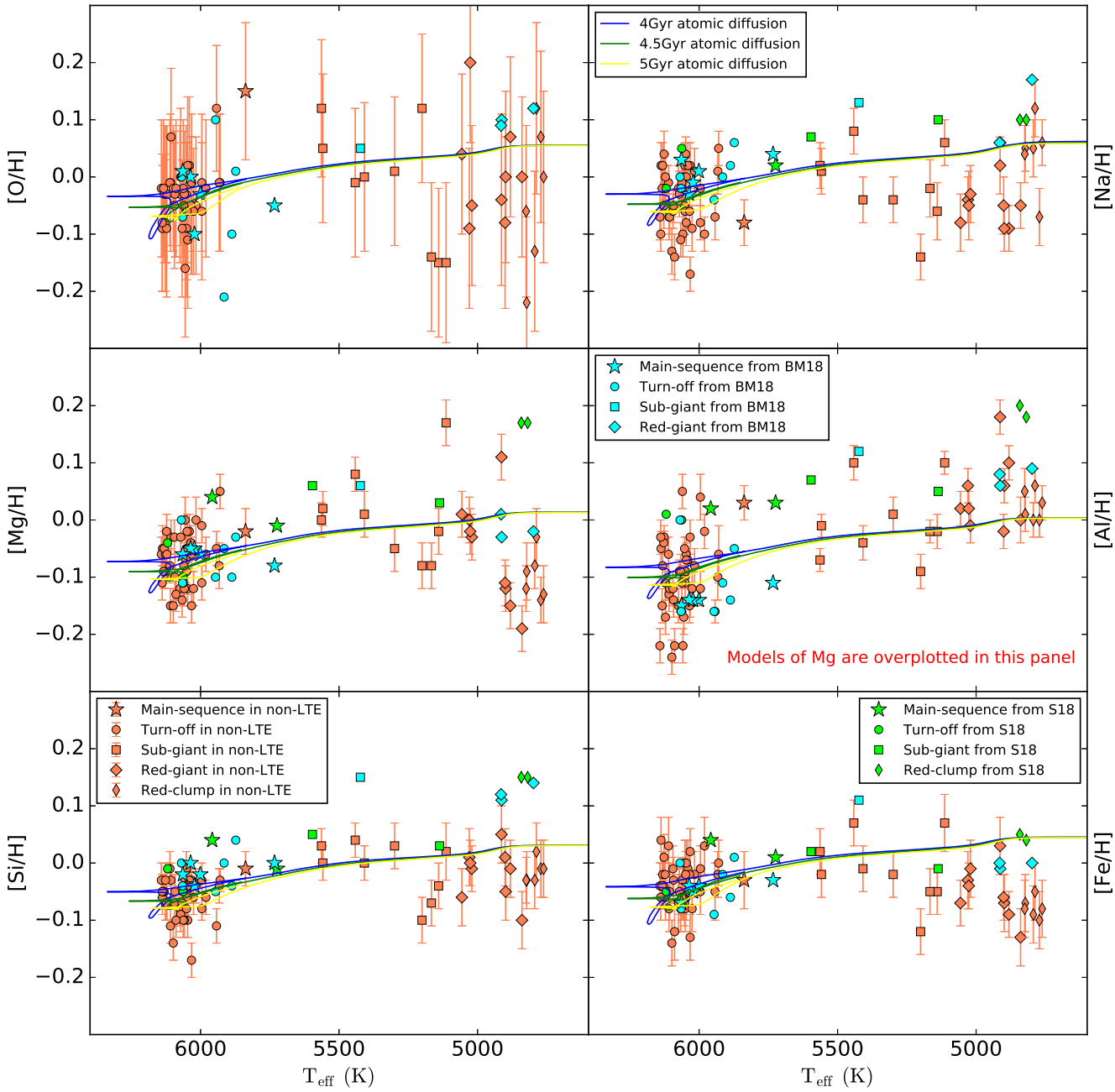

Figure 9. Non-LTE Abundances [X/H] as a function of effective temperature for individual M67 stars. We overplot surface abundance isochrones from atomic diffusion models with solar metallicity and different evolution ages. Al is not shown in the model-data comparison, since it has been neglected in the model output. Instead, we overplot the models of Mg on the Al measurements. We also overplot the abundance results from Souto et al. (2018) and Bertelli Motta et al. (2018). Stars in different evolutionary states are marked with different symbols.

(MIST; Dotter 2016; Choi et al. 2016) have included atomic diffusion, overshooting mixing and turbulent diffusion. Furthermore, the models are calculated with radiative acceleration, which acts differently on different chemical species and can thus potentially explain different abundance trends for the different elements under consideration.

In Fig. 9 and Fig. 10, we overplot the stellar evolutionary models on our results for the surface abundances versus effective temperature and gravity, respectively. Since Al has been neglected in the model output, models of Al are not shown in the model-data comparison. We note that Al is expected to behave similarly to the other elements (see e.g. Bertelli Motta et al. 2018). We thus overplot the models of Mg on the Al measurements instead. Since the zero-points of the models are not relevant here, and we are more interested in the effect of atomic diffusion on their relative surface abundances, small arbitrary offsets have been applied to all the model abundances so as to generally match our abundance measurements for the turn-off stars.

Fig. 10 most clearly illustrates the evolutionary effects predicted by the models; the model abundances decrease on the main-

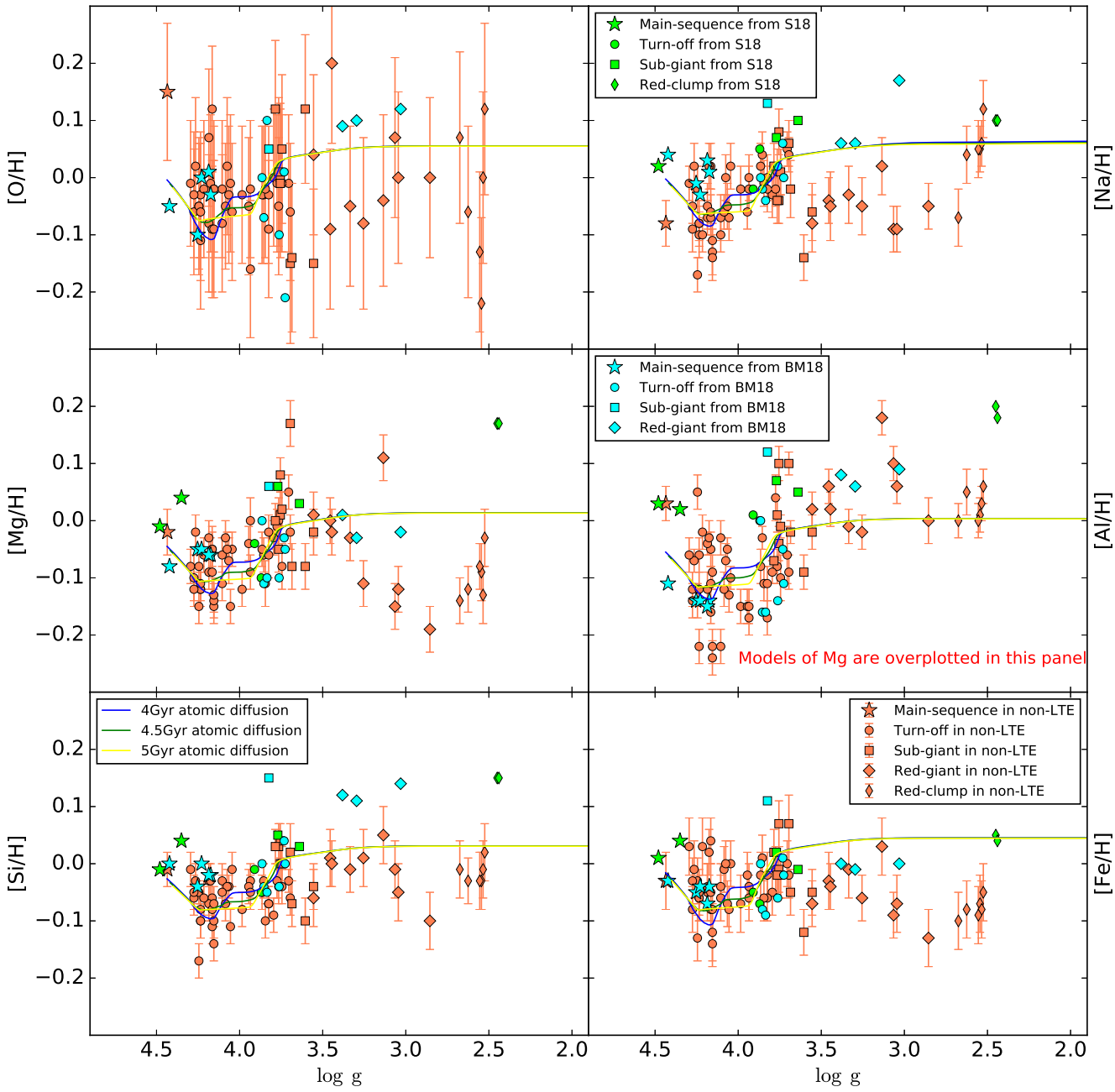

Figure 10. Non-LTE Abundances [X/H] as a function of log g for individual M67 stars. We overplot surface abundance isochrones from atomic diffusion models with solar metallicity and different evolution ages. Al is not shown in the model-data comparison, since it has been neglected in the model output. Instead, we overplot the models of Mg on the Al measurements. We also overplot the abundance results from Souto et al. (2018) and Bertelli Motta et al. (2018). Stars in different evolutionary states are marked with different symbols.

sequence with increasing mass to reach a minimum around the turn-off; the severity of this depletion is age-dependent, being more severe for older ages. Moving to later evolutionary stages (lower surface gravity and effective temperature), the elements are brought back up to the surface by convective mixing (i.e. the first dredge-up), and the surface abundance depletion becomes less severe. At the base of the red giant branch, the surface abundances are restored to the original composition; the models actually predict a slight increase in the surface abundances over the initial values as a result of hydrogen being consumed during central H-burning.

We now highlight some interesting aspects evident from the comparison between our observed abundances and the model predictions in Fig. 10. We note that the initial decrease with increasing mass cannot be tested with our data, since there are too few main sequence stars. However, there is a satisfying morphological agreement with the models in the dredge-up pattern from the turn-off to the subgiant branch. However, our abundance measurements of the red-giant and red-clump stars (with effective temperature less than 5100 K) do not fit the predicted trend very well, even considering the abundance errors, for all elements except possibly Al. One pos-

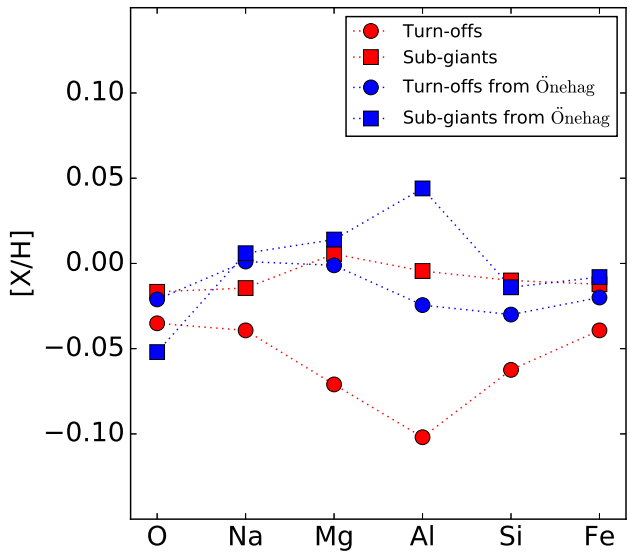

Figure 11. A comparison between our non-LTE abundance patterns of turn-off, sub-giant and giant stars and those from Önehag's turn-off and early sub-giant stars.

sible reason for this discrepancy could be that the stellar parameters for these giant stars are poorly determined (see Fig. 2). Problems in the main stellar parameters will propagate the systematic offsets to the individual stellar abundances. However, this can not be the single contribution to explain this discrepancy, since the systematic offsets propagating to different elements may have different correction directions.

5.2 Comparison to other studies

In this section, we compare our abundance results to previous high-resolution studies of M67. Table 2 summarises the target selection and spectroscopic quality for seven literature studies. We also include the mean abundance ratios determined in those studies. We compare these results, which were mainly based on equivalent-widths and under the assumption of LTE, with our own results, which are based on spectral line fitting and under non-LTE.

Our mean [Fe/H] value in non-LTE for M67 is consistent with the value of Tautvaišiene et al. (2000), Önehag et al. (2014) and Bertelli Motta et al. (2018), but is slightly lower than those determined from the other studies shown in Table 2. Generally all the results are comparable with solar metallicity to within their respective errors. However, some disagreements between other measured abundances from different studies do exist.

Overall, our abundance ratios in non-LTE are close to solar, and are systematically lower than those studies wherein only giants have been analyzed, namely Tautvaišiene et al. (2000), Yong et al. (2005), Pancino et al. (2010) and Friel et al. (2010). The abundance results that are mainly based on unevolved stars from Randich et al. (2006), Pace et al. (2008), Önehag et al. (2014), Bertelli Motta et al. (2018) and Souto et al. (2018) are more consistent with those presented in this work.

The differences in the abundances determined in this work and those presented elsewhere could be the result of a variety of factors, including the choice of atmospheric model, abundance calculation code, the determined stellar parameters, the choice of $\log gf$ values and line lists, the choice of solar reference abundances and non-LTE effects. In this work, all of the abundances are determined by spectrum synthesis, which are more reliable and accurate, especially when the lines are blended, than the traditional equivalent width analysis. We note, too, that our results benefit from being based on the largest sample of high-quality spectra yet published, covering turn-off, sub-giant star, red giant and red clump stars compared with other studies, whose abundances are derived based on a smaller number of objects.

We compare the results of Önehag et al. (2014) with those presented in this work in Fig. 11. Önehag et al. (2014) analysed 14 turn-offs and sub-giants using high resolution spectra ($R \approx 50,000$), an analysis based on equivalent-widths and under the assumption of LTE. Their abundances were derived for each spectral line individually relative to those of the solar proxy M67-1194. Our mean chemical abundances are typically lower than the ones from Önehag et al. (2014). However, in that work as well as our own, we find that the abundances in sub-giants are enhanced relative to those in turn-offs. This enhancement is smaller in the results of Önehag et al. (2014) than in this work; this may be because the sub-giants used in that work are located very close to the turn-off, whereas here they span the full subgiant branch. These overall increasing abundances from turn-offs to sub-giants could be a signature for possible diffusion process (Sect. 5.1).

Recent studies by Bertelli Motta et al. (2018) and Souto et al. (2018) both investigated the presence of atomic diffusion effects in M67 by analysing the member stars across different evolutionary phases. We overplot their results in Fig. 9 and Fig. 10. Their inferred abundance patterns show an overall agreement with the atomic diffusion models from Dotter et al. (2017) and their abundance distributions for turn-off and subgiant stars are generally consistent with our non-LTE results, with some notable exceptions. We note that the other two studies show no evidence of low abundances for red giants compared to less evolved stars, as seen in our data for O, Na, Mg, and Fe. This reinforces our suspicion that our giant star abundances are not accurate (see Sect. 5.1)

Looking at individual elements, the measured [O/H] from Bertelli Motta et al. (2018) also presents a fairly large scatter, which the authors ascribe to telluric blending and weakness of the [OI] line at 630nm. However, this line is not expected to suffer large non-LTE effects and the agreement with our non-LTE abundances is significantly better than with our LTE abundances. The LTE [Na/H] abundances derived by the other two groups are consistently somewhat higher than our non-LTE abundance trend and Bertelli Motta et al. (2018) estimate that their Na LTE abundances are indeed overestimated by $0.1 - 0.15$ dex.

The [Mg/H] abundances agree well for unevolved stars, while the red giants show a disagreement of > 0.2 dex between the three groups, which cannot be attributed to non-LTE effects. For [Al/H], our abundances tend to fall between results of the other two groups, but there is satisfactory agreement on the increasing abundance trend with evolutionary phase. The [Si/H] abundances of the other two groups are higher than ours and the predicted abundance trend slightly steeper. We note that Bertelli Motta et al. (2018) suspect that their Si analysis suffers from an unknown bias, elevating the abundances in giants with respect to dwarfs. The [Fe/H] abundances are in good agreement between all three studies for turn-off stars and subgiants, but not for giants, as mentioned above.

Table 2. The comparison of average abundances in common for M67 based on high resolution spectroscopy. The total number of stars analyzed in each study is given by #.

	#	R	SNR	[Fe/H]	[O/Fe]	[Na/Fe]	[Mg/Fe]	[Al/Fe]	[Si/Fe]
NLTE[1]	66	42000	50–150	−0.04 ± 0.04	+0.04 ± 0.09	+0.03 ± 0.05	+0.00 ± 0.05	+0.01 ± 0.07	+0.02 ± 0.03
T00[2]	9	30000–60000	≥ 100	−0.03 ± 0.03	+0.02 ± 0.06	+0.19 ± 0.06	+0.10 ± 0.04	+0.14 ± 0.04	+0.10 ± 0.05
Y05[3]	3	28000	30–100	+0.02 ± 0.14	+0.07 ± 0.05	+0.30 ± 0.10	+0.16 ± 0.08	+0.17 ± 0.05	+0.09 ± 0.11
R06[4]	10	45000	90–180	+0.03 ± 0.03	+0.01 ± 0.03	+0.05 ± 0.07	+0.00 ± 0.02	−0.05 ± 0.04	+0.02 ± 0.04
P08[5]	6	100000	≃ 80	+0.03 ± 0.04	−0.07 ± 0.09	−0.02 ± 0.07	-	−0.03 ± 0.11	−0.03 ± 0.06
P10[6]	3	30000	50–100	+0.05 ± 0.02	+0.04 ± 0.10	+0.08 ± 0.09	+0.27 ± 0.04	+0.03 ± 0.02	+0.10 ± 0.02
F10[7]	3	30000	150–180	+0.03 ± 0.07	−0.16 ± 0.05	+0.13 ± 0.10	+0.05 ± 0.03	+0.11 ± 0.07	+0.18 ± 0.04
Ö14[8]	14	50000	150	−0.02 ± 0.04	−0.02 ± 0.05	+0.02 ± 0.03	+0.02 ± 0.02	+0.02 ± 0.04	−0.01 ± 0.02
BM18[9]	15	47000	–	−0.02 ± 0.05	+0.02 ± 0.09	+0.06 ± 0.04	−0.02 ± 0.02	−0.04 ± 0.07	+0.05 ± 0.04
S18[10]	8	22500	120–956	+0.00 ± 0.04	–	+0.06 ± 0.04	+0.04 ± 0.06	+0.07 ± 0.05	+0.04 ± 0.04

Notes. (1) This work (2) Tautvaišiene et al. (2000) analysed 6 red-clump stars and 3 giant stars. (3) Yong et al. (2005) analysed 3 red-clump stars. (4) Randich et al. (2006) analysed 8 dwarfs and 2 slightly evolved stars. (5) Pace et al. (2008) analysed 6 main-sequence stars. (6) Pancino et al. (2010) analysed 3 red-clump stars. (7) Friel et al. (2010) analysed 3 red-clump stars. (8) Önehag et al. (2014) analysed 14 stars whose 6 are located on the main-sequence, 3 are at the turn-off point, and 5 are on the early sub-giant branch. (9) Bertelli Motta et al. (2018) analysed 15 stars whose 5 are located on the main-sequence, 6 are at the turn-off phase, 1 are on the sub-giant branch and 3 are on the red-giant branch. (10) Souto et al. (2018) analysed 8 stars, including two main-sequence stars, two turn-off stars, two sub-giants and two red-clump stars

6 CONCLUSION

We have presented a comprehensive determination of the M67 elemental abundances of lithium, oxygen, sodium, magnesium, aluminium, silicon, and iron. We analysed lines using non-LTE and LTE calculations with 1D hydrostatic MARCS model atmospheres based on high resolution, high quality spectra from the GALAH survey.

We have accounted for non-LTE effects in the line formation of different elements. For lithium, non-LTE effects are not prominent. However, the large scatter (0.21 dex) in lithium abundances in stars with similar stellar parameters (i.e. mass, metallicity and age) may indicate that the stars in this cluster could have different initial angular momentums to which would naturally result in different levels of lithium depletion. In addition, we found a lithium-rich sub-giant in our sample, which we note is a spectroscopic binary. It could be a potential candidate to study unusual lithium induced by tidal effects.

We found that the scatter in mean abundance is reduced for all the elements under the assumption of non-LTE, compared to under LTE, because non-LTE analyses flattens the trends in surface abundances with effective temperature (see Fig. 7). However, abundance differences between stars in different evolutionary phases are not fully erased by non-LTE effects. The star-to-star abundance scatter for similar stars appears largely unaffected by non-LTE analysis.

We compared our observed abundance trends with the trends predicted by the atomic diffusion model of Dotter et al. (2017), assuming solar metallicity and approximately solar age. Our non-LTE results match well with model prediction for turn-off stars and sub-giants within the errors, however, they fail to meet the predicted trend for later phase red-giant and red-clump stars. One possible reason for this differences could be caused by the poor determination of stellar parameters for those giant stars.

To increase the accuracy of our abundance measurements further, 3D hydrodynamical model atmospheres should be considered. Such modelling is important for late type atmospheres, where the spectral line form at the top of the convective region, and eliminates the need for the artificial broadening parameters, such as microturbulence and macroturbulence. (e.g. Asplund et al. 2000). Performing a 3D non-LTE study is beyond the scope of the present work. We note however that 3D corrections for the same lines can go in opposite directions for turn-offs and giants. Consequently, it is possible that a 3D non-LTE analysis would find significantly flatter or steeper abundance trends than those presented in Sect. 4.3 (Korn et al. 2007).

Finally, we underline the necessity to include accurate non-LTE corrections in order to obtain more reliable abundances to study abundance evolution and chemical tagging. Our analysis shows that, due to the potential influence of both systematic abundance errors and of stellar evolution effects, the method of connecting stars in the field to a common birth location by chemical similarity is significantly more reliable for stars in the same evolutionary phase.

ACKNOWLEDGEMENTS

XDG, KL, and AMA acknowledge funds from the Alexander von Humboldt Foundation in the framework of the Sofja Kovalevskaja Award endowed by the Federal Ministry of Education and Research, and KL also acknowledges funds from the Swedish Research Council (grant 2015-004153) and Marie Skłodowska Curie Actions (cofund project INCA 600398). TZ acknowledges financial support of the Slovenian Research Agency (research core funding No. P1-0188). SLM acknowledges support from the Australian Research Council through grant DE140100598. Parts of this research were conducted by the Australian Research Council Centre of Excellence for All Sky Astrophysics in 3 Dimensions (ASTRO 3D), through project number CE170100013. This work is also based on data acquired from the Australian Astronomical Telescope. We acknowledge the traditional owners of the land on which the AAT stands, the Gamilaraay people, and pay our respects to elders past and present. This research has made use of the SIMBAD database, operated at CDS, Strasbourg, France. We thank an anonymous referee for many insightful comments that helped improve the manuscript.

REFERENCES

Amarsi A. M., Asplund M., 2017, MNRAS, 464, 264
Amarsi A. M., Asplund M., Collet R., Leenaarts J., 2015, MNRAS, 454, L11
Amarsi A. M., Asplund M., Collet R., Leenaarts J., 2016a, MNRAS, 455, 3735
Amarsi A. M., Lind K., Asplund M., Barklem P. S., Collet R., 2016b, MNRAS, 463, 1518
Asplund M., 2005, ARA&A, 43, 481
Asplund M., Nordlund Å., Trampedach R., Allende Prieto C., Stein R. F., 2000, A&A, 359, 729
Asplund M., Grevesse N., Sauval A. J., Scott P., 2009, ARA&A, 47, 481
Badnell N. R., 2011, Computer Physics Communications, 182, 1528
Balachandran S., 1995, ApJ, 446, 203
Barklem P. S., 2016a, A&A Rev., 24, 9
Barklem P. S., 2016b, Phys. Rev. A, 93, 042705
Barklem P. S., Belyaev A. K., Asplund M., 2003, A&A, 409, L1
Barklem P. S., Belyaev A. K., Dickinson A. S., Gadéa F. X., 2010, A&A, 519, A20
Barklem P. S., Belyaev A. K., Spielfiedel A., Guitou M., Feautrier N., 2012, A&A, 541, A80
Bautista M. A., 1997, A&AS, 122, 167
Belyaev A. K., 2013, A&A, 560, A60
Belyaev A. K., Barklem P. S., 2003, Phys. Rev. A, 68, 062703
Belyaev A. K., Yakovleva S. A., Barklem P. S., 2014, A&A, 572, A103
Bergemann M., Collet R., Amarsi A. M., Kovalev M., Ruchti G., Magic Z., 2017, ApJ, 847, 15
Berrington K. A., Burke P. G., Chang J. J., Chivers A. T., Robb W. D., Taylor K. T., 1974, Computer Physics Communications, 8, 149
Bertelli Motta C., Salaris M., Pasquali A., Grebel E. K., 2017, MNRAS, 466, 2161
Bertelli Motta C., et al., 2018, MNRAS, 478, 425
Brault J., Neckel H., 1987, Tape copy from KIS IDL library
Bressan A., Marigo P., Girardi L., Salasnich B., Dal Cero C., Rubele S., Nanni A., 2012, MNRAS, 427, 127
Buder S., et al., 2018, MNRAS, 478, 4513
Burke P. G., Hibbert A., Robb W. D., 1971, Journal of Physics B Atomic Molecular Physics, 4, 153
Canto Martins B. L., Lèbre A., de Laverny P., Melo C. H. F., Do Nascimento Jr. J. D., Richard O., de Medeiros J. R., 2006, A&A, 451, 993
Chen Y., Girardi L., Bressan A., Marigo P., Barbieri M., Kong X., 2014, MNRAS, 444, 2525
Choi J., Dotter A., Conroy C., Cantiello M., Paxton B., Johnson B. D., 2016, ApJ, 823, 102
Dalton G., et al., 2012, in Ground-based and Airborne Instrumentation for Astronomy IV. p. 84460P, doi:10.1117/12.925950
De Silva G. M., Sneden C., Paulson D. B., Asplund M., Bland-Hawthorn J., Bessell M. S., Freeman K. C., 2006, AJ, 131, 455
De Silva G. M., Freeman K. C., Asplund M., Bland-Hawthorn J., Bessell M. S., Collet R., 2007, AJ, 133, 1161
De Silva G. M., et al., 2015, MNRAS, 449, 2604
Dotter A., 2016, ApJS, 222, 8
Dotter A., Conroy C., Cargile P., Asplund M., 2017, ApJ, 840, 99
Drawin H.-W., 1968, Zeitschrift fur Physik, 211, 404
Duong L., et al., 2018, preprint, (arXiv:1801.01514)
Feng Y., Krumholz M. R., 2014, Nature, 513, 523
Freeman K., Bland-Hawthorn J., 2002, ARA&A, 40, 487
Friel E. D., Jacobson H. R., Pilachowski C. A., 2010, AJ, 139, 1942
García Pérez A. E., Asplund M., Primas F., Nissen P. E., Gustafsson B., 2006, A&A, 451, 621
Geller A. M., Latham D. W., Mathieu R. D., 2015, AJ, 150, 97
Gilmore G., et al., 2012, The Messenger, 147, 25
Gray D. F., 2005, The Observation and Analysis of Stellar Photospheres
Grevesse N., Asplund M., Sauval A. J., 2007, Space Sci. Rev., 130, 105
Gruyters P., Nordlander T., Korn A. J., 2014, A&A, 567, A72
Gruyters P., et al., 2016, A&A, 589, A61
Gustafsson B., Edvardsson B., Eriksson K., Jørgensen U. G., Nordlund Å., Plez B., 2008, A&A, 486, 951
Gustafsson B., Church R. P., Davies M. B., Rickman H., 2016, A&A, 593, A85
Hobbs L. M., Thorburn J. A., 1991, AJ, 102, 1070
Holtzman J. A., et al., 2015, AJ, 150, 148
Kiselman D., 1993, A&A, 275
Korn A. J., Grundahl F., Richard O., Mashonkina L., Barklem P. S., Collet R., Gustafsson B., Piskunov N., 2007, ApJ, 671, 402
Kos J., et al., 2017, MNRAS, 464, 1259
Kos J., et al., 2018, MNRAS, 473, 4612
Kunder A., et al., 2017, AJ, 153, 75
Kurucz R. L., 1995, in Adelman S. J., Wiese W. L., eds, Astronomical Society of the Pacific Conference Series Vol. 78, Astrophysical Applications of Powerful New Databases. p. 205
Lambert D. L., 1993, Physica Scripta Volume T, 47, 186
Lind K., Asplund M., Barklem P. S., 2009a, A&A, 503, 541
Lind K., Primas F., Charbonnel C., Grundahl F., Asplund M., 2009b, A&A, 503, 545
Lind K., Asplund M., Barklem P. S., Belyaev A. K., 2011, A&A, 528, A103
Lind K., Bergemann M., Asplund M., 2012, MNRAS, 427, 50
MacLean B. T., De Silva G. M., Lattanzio J., 2015, MNRAS, 446, 3556
Magrini L., et al., 2014, A&A, 563, A44
Majewski S. R., et al., 2017, AJ, 154, 94
Martell S. L., et al., 2017, MNRAS, 465, 3203
Martin A. J., Stift M. J., Fossati L., Bagnulo S., Scalia C., Leone F., Smalley B., 2017, MNRAS, 466, 613
Mathieu R. D., Latham D. W., Griffin R. F., 1990, AJ, 100, 1859
Michaud G., Fontaine G., Beaudet G., 1984, ApJ, 282, 206
Nordlander T., Lind K., 2017, preprint, (arXiv:1708.01949)
Nordlander T., Korn A. J., Richard O., Lind K., 2012, ApJ, 753, 48
Önehag A., Korn A., Gustafsson B., Stempels E., Vandenberg D. A., 2011, A&A, 528, A85
Önehag A., Gustafsson B., Korn A., 2014, A&A, 562, A102
Osorio Y., Barklem P. S., 2016, A&A, 586, A120
Osorio Y., Barklem P. S., Lind K., Belyaev A. K., Spielfiedel A., Guitou M., Feautrier N., 2015, A&A, 579, A53
Pace G., Pasquini L., François P., 2008, A&A, 489, 403
Pace G., Castro M., Meléndez J., Théado S., do Nascimento Jr. J.-D., 2012, A&A, 541, A150
Pancino E., Carrera R., Rossetti E., Gallart C., 2010, A&A, 511, A56
Pasquini L., Biazzo K., Bonifacio P., Randich S., Bedin L. R., 2008, A&A, 489, 677
Peach G., Saraph H. E., Seaton M. J., 1988, Journal of Physics B Atomic Molecular Physics, 21, 3669
Pichardo B., Moreno E., Allen C., Bedin L. R., Bellini A., Pasquini L., 2012, AJ, 143, 73
Pinsonneault M. H., 2010, in Charbonnel C., Tosi M., Primas F., Chiappini C., eds, IAU Symposium Vol. 268, Light Elements in the Universe. pp 375–380 (arXiv:1001.3864), doi:10.1017/S1743921310004497
Piskunov N., Valenti J. A., 2017, A&A, 597, A16
Prantzos N., Charbonnel C., 2006, A&A, 458, 135
Randich S., Sestito P., Primas F., Pallavicini R., Pasquini L., 2006, A&A, 450, 557
Reader J., Kramida A., Ralchenko Y., 2012, in American Astronomical Society Meeting Abstracts #219. p. 443.01
Sanders W. L., 1977, A&AS, 27, 89
Sarajedini A., Dotter A., Kirkpatrick A., 2009, ApJ, 698, 1872
Schuler S. C., King J. R., The L.-S., 2009, ApJ, 701, 837
Scott P., et al., 2015a, A&A, 573, A25
Scott P., Asplund M., Grevesse N., Bergemann M., Sauval A. J., 2015b, A&A, 573, A26
Sharma S., et al., 2017, preprint, (arXiv:1707.05753)
Sheinis A., et al., 2015, Journal of Astronomical Telescopes, Instruments, and Systems, 1, 035002
Skrutskie M. F., et al., 2006, AJ, 131, 1163
Smiljanic R., et al., 2016, A&A, 589, A115
Souto D., et al., 2018, ApJ, 857, 14
Steenbock W., Holweger H., 1984, A&A, 130, 319

Takeda Y., 2003, A&A, 402, 343
Tang J., Bressan A., Rosenfield P., Slemer A., Marigo P., Girardi L., Bianchi L., 2014, MNRAS, 445, 4287
Tautvaišiene G., Edvardsson B., Tuominen I., Ilyin I., 2000, A&A, 360, 499
Turcotte S., Richer J., Michaud G., Iglesias C. A., Rogers F. J., 1998, ApJ, 504, 539
Villanova S., Carraro G., Saviane I., 2009, A&A, 504, 845
Wenger M., et al., 2000, A&AS, 143, 9
Wittenmyer R. A., et al., 2017, preprint, (arXiv:1712.06774)
Yadav R. K. S., et al., 2008, A&A, 484, 609
Yakut K., et al., 2009, A&A, 503, 165
Yong D., Carney B. W., Teixera de Almeida M. L., 2005, AJ, 130, 597
de Jong R. S., et al., 2012, in Ground-based and Airborne Instrumentation for Astronomy IV. p. 84460T (arXiv:1206.6885), doi:10.1117/12.926239
van Regemorter H., 1962, ApJ, 136, 906

APPENDIX A: TABLES OF THE FUNDAMENTAL PARAMETERS

APPENDIX B: TABLES OF THE CHEMICAL ABUNDANCES

Table A1. Fundamental parameters of the sample stars from the spectroscopic analysis of GALAH data. The columes from left to right show the GALAH ID, the star identifier in the 2MASS catalogue, the type of the star,the effective temperature, the surface gravity, the stellar metallicity, the micro-turbulence, the projected surface rotational velocity and radial velocity. Note that $v \sin \iota$ is actually a combined measurement from both $v \sin \iota$ and $v_{\rm mac}$, since they have a degenerate influence effect on spectral line broadening and cannot been disentangled.

GALAH ID	2MASS ID	Group	$T_{\rm eff}$ (K)	$\log g$	Metallicity	ξ (km s^{-1})	$v \sin \iota$ (km s^{-1})	RV (km s^{-1})
6561552	08505344 + 1144346	Main-sequence	5837	4.43	−0.05	0.93	8.81	34.65
6560101	08511833 + 1143251	Turn-off	6141	4.11	−0.07	1.07	7.70	34.06
6577714	08514522 + 1156552	Turn-off	6138	4.11	−0.08	1.09	8.30	34.62
6554484	08514493 + 1138589	Turn-off	6137	4.16	0.01	1.08	7.68	33.36
6577148	08505439 + 1156290	Turn-off	6133	3.93	−0.08	1.08	9.20	33.97
6569011	08511534 + 1150143	Turn-off	6131	3.87	−0.05	1.08	9.15	34.14
6565966	08504766 + 1147525	Turn-off	6127	4.18	−0.06	1.08	7.76	34.85
6565326	08511476 + 1147238	Turn-off	6126	3.86	−0.03	1.08	9.54	35.38
6574584	08514122 + 1154290	Turn-off	6122	3.82	−0.07	1.07	10.32	34.50
6571679	08512830 + 1152175	Turn-off	6121	3.82	−0.11	1.07	8.85	34.49
6567547	08514082 + 1149055	Turn-off	6110	4.30	0.02	1.05	8.35	34.54
6555602	08505973 + 1139524	Turn-off	6108	4.05	−0.10	1.07	7.07	33.75
6561039	08514597 + 1144093	Turn-off	6106	4.18	−0.08	1.06	9.09	33.75
6570179	08505474 + 1151093	Turn-off	6098	4.16	−0.15	1.05	7.40	34.61
6564123	08514641 + 1146267	Turn-off	6094	4.09	−0.04	1.05	8.91	34.53
6573044	08513119 + 1153179	Turn-off	6092	4.28	−0.07	1.02	7.37	34.02
6575508	08505762 + 1155147	Turn-off	6088	4.16	−0.14	1.03	7.94	34.19
6558150	08514465 + 1141510	Turn-off	6074	3.98	−0.12	1.03	9.18	33.18
6568768	08513923 + 1150038	Turn-off	6071	3.79	−0.11	1.04	14.49	36.38
6573727	08505600 + 1153520	Turn-off	6066	4.16	−0.11	1.03	7.85	35.18
6573191	08512742 + 1153265	Turn-off	6062	3.84	−0.10	1.04	7.89	33.98
6572337	08512015 + 1152479	Turn-off	6060	4.24	−0.03	1.05	7.83	34.24
6569861	08510857 + 1150530	Turn-off	6058	4.24	−0.09	1.03	7.21	35.74
6564445	08512205 + 1146409	Turn-off	6055	3.93	−0.08	1.04	9.63	35.61
6567617	08512595 + 1149089	Turn-off	6052	4.07	−0.10	1.02	9.09	35.12
6559497	08511810 + 1142547	Turn-off	6051	4.05	−0.03	1.04	7.12	34.15
6568479	08520785 + 1149500	Turn-off	6050	4.16	−0.10	1.04	8.72	33.72
6572560	08515963 + 1152576	Turn-off	6048	3.69	−0.07	1.02	8.48	34.32
6572187	08512552 + 1152388	Turn-off	6046	4.07	−0.02	1.03	7.53	34.95
6560653	08513012 + 1143498	Turn-off	6046	4.24	−0.09	1.02	8.19	34.35
6567233	08511164 + 1148505	Turn-off	6040	4.26	−0.02	1.02	6.58	36.38
6569167	08520741 + 1150221	Turn-off	6034	3.94	−0.05	1.02	8.23	35.22
6565967	08510156 + 1147501	Turn-off	6032	4.18	−0.01	1.02	6.68	33.59
6562672	08504760 + 1145228	Turn-off	6032	4.24	−0.16	1.00	6.46	34.56
6571851	08510492 + 1152261	Turn-off	6025	4.28	−0.10	1.01	6.95	35.13
6568307	08514914 + 1149435	Turn-off	6016	3.76	−0.06	1.01	8.38	34.80
8436138	08504976 + 1154244	Turn-off	5995	4.24	−0.09	0.99	6.64	33.53
6571594	08505569 + 1152146	Turn-off	5995	3.77	−0.04	1.00	7.53	34.62
6579199	08520330 + 1158046	Turn-off	5980	4.22	0.01	0.99	6.64	33.66
6562188	08512080 + 1145024	Turn-off	5942	4.16	−0.08	0.96	8.51	35.09
6567847	08511854 + 1149214	Turn-off	5932	3.74	−0.06	0.97	7.35	35.08
6563234	08510325 + 1145473	Turn-off	5929	3.70	−0.03	0.98	6.72	35.63
9077970	08513540 + 1157564	Sub-giant	5563	3.78	−0.01	0.89	7.00	33.71
6568921	08510106 + 1150108	Sub-giant	5558	3.74	−0.05	0.89	6.49	33.23
6574583	08510018 + 1154321	Sub-giant	5441	3.75	0.04	0.90	7.18	34.13
6562991	08521134 + 1145380	Sub-giant	5408	3.75	−0.03	0.91	7.40	33.40
6569862	08511564 + 1150561	Sub-giant	5299	3.76	−0.04	0.93	6.16	34.51
6567693	08504994 + 1149127	Sub-giant	5200	3.61	−0.15	0.97	6.19	34.21
6577630	08514883 + 1156511	Sub-giant	5166	3.68	−0.05	0.98	8.01	34.92
6562765	08512935 + 1145275	Sub-giant	5140	3.55	−0.07	1.00	6.74	33.81
6569012	08515611 + 1150147	Sub-giant	5113	3.69	0.07	1.04	7.41	35.89
6571766	08505816 + 1152223	Red-giant	5056	3.55	−0.08	1.05	5.85	34.58
6565104	08510839 + 1147121	Red-giant	5029	3.45	−0.04	1.06	5.52	34.27
6579331	08511897 + 1158110	Red-giant	5026	3.44	−0.04	1.07	6.47	34.69
6573364	08513577 + 1153347	Red-giant	5020	3.33	−0.05	1.07	7.07	34.76
6563655	08512156 + 1146061	Red-giant	4913	3.13	0.04	1.17	6.68	35.28
6570514	08514235 + 1151230	Red-giant	4900	3.25	−0.02	1.18	7.66	34.85
6568851	08514234 + 1150076	Red-giant	4898	3.04	−0.05	1.17	7.68	34.73
6565879	08514507 + 1147459	Red-giant	4881	3.06	−0.07	1.19	7.49	32.79
6569711	08511704 + 1150464	Red-giant	4839	2.86	−0.12	1.24	6.46	34.35
6575356	08515952 + 1155049	Red-clump	4824	2.62	−0.08	1.23	7.78	35.38
6577481	08514388 + 1156425	Red-clump	4822	2.54	−0.08	1.21	7.56	33.82
6573728	08512618 + 1153520	Red-clump	4793	2.55	−0.10	1.24	6.98	34.90
6566179	08512280 + 1148016	Red-clump	4787	2.52	−0.06	1.25	7.55	34.23
6569393	08512898 + 1150330	Red-clump	4771	2.67	−0.08	1.28	7.48	34.20
6572270	08511269 + 1152423	Red-clump	4761	2.53	−0.11	1.24	6.94	35.14

Table B1. Non-LTE chemical abundances of the sample stars in M67. Abundances were derived relative to non-LTE values of solar analysed in this work.

GALAH ID	Group	A(Li)$_{NLTE}$	[O/H]$_{NLTE}$	[Na/H]$_{NLTE}$	[Mg/H]$_{NLTE}$	[Al/H]$_{NLTE}$	[Si/H]$_{NLTE}$	[Fe/H]$_{NLTE}$
6561552	Main-sequence	–	0.15 ± 0.12	−0.08 ± 0.04	−0.02 ± 0.04	0.03 ± 0.03	−0.01 ± 0.03	−0.03 ± 0.05
6560101	Turn-off	2.68 ± 0.05	−0.02 ± 0.12	−0.07 ± 0.04	−0.06 ± 0.03	−0.22 ± 0.03	−0.03 ± 0.03	−0.04 ± 0.04
6577714	Turn-off	2.66 ± 0.05	−0.08 ± 0.12	−0.10 ± 0.03	−0.11 ± 0.03	−0.03 ± 0.03	−0.05 ± 0.03	−0.06 ± 0.04
6554484	Turn-off	2.68 ± 0.05	−0.09 ± 0.12	0.02 ± 0.04	−0.05 ± 0.03	−0.05 ± 0.02	−0.06 ± 0.03	0.04 ± 0.04
6577148	Turn-off	–	−0.02 ± 0.11	−0.02 ± 0.04	−0.09 ± 0.04	−0.15 ± 0.03	−0.05 ± 0.03	−0.04 ± 0.04
6569011	Turn-off	2.34 ± 0.05	−0.03 ± 0.12	0.02 ± 0.04	−0.05 ± 0.03	−0.08 ± 0.03	−0.05 ± 0.03	−0.02 ± 0.04
6565966	Turn-off	2.54 ± 0.05	−0.08 ± 0.12	−0.05 ± 0.04	−0.09 ± 0.03	−0.04 ± 0.03	−0.07 ± 0.03	−0.04 ± 0.04
6565326	Turn-off	2.42 ± 0.05	−0.03 ± 0.12	0.04 ± 0.04	−0.06 ± 0.03	−0.03 ± 0.02	−0.03 ± 0.03	0.01 ± 0.04
6574584	Turn-off	–	−0.09 ± 0.12	−0.02 ± 0.04	−0.02 ± 0.03	−0.11 ± 0.03	−0.07 ± 0.03	−0.02 ± 0.04
6571679	Turn-off	–	−0.03 ± 0.12	0.00 ± 0.04	−0.06 ± 0.04	−0.17 ± 0.03	−0.07 ± 0.03	−0.06 ± 0.04
6567547	Turn-off	2.52 ± 0.05	−0.01 ± 0.12	−0.01 ± 0.04	−0.08 ± 0.03	−0.06 ± 0.03	−0.01 ± 0.03	0.03 ± 0.04
6555602	Turn-off	–	−0.01 ± 0.12	−0.07 ± 0.03	−0.15 ± 0.03	−0.13 ± 0.03	−0.11 ± 0.03	−0.08 ± 0.05
6561039	Turn-off	2.70 ± 0.05	0.07 ± 0.11	−0.07 ± 0.04	−0.03 ± 0.03	−0.12 ± 0.03	−0.03 ± 0.03	−0.05 ± 0.04
6570179	Turn-off	2.44 ± 0.05	−0.02 ± 0.11	−0.13 ± 0.03	−0.15 ± 0.03	−0.24 ± 0.03	−0.14 ± 0.03	−0.14 ± 0.05
6564123	Turn-off	2.38 ± 0.05	−0.05 ± 0.11	−0.06 ± 0.03	−0.03 ± 0.03	−0.12 ± 0.03	−0.07 ± 0.03	−0.01 ± 0.04
6573044	Turn-off	2.45 ± 0.05	−0.03 ± 0.12	−0.05 ± 0.04	−0.10 ± 0.03	−0.14 ± 0.03	−0.05 ± 0.03	−0.03 ± 0.05
6575508	Turn-off	2.23 ± 0.05	−0.02 ± 0.11	−0.14 ± 0.03	−0.13 ± 0.04	−0.22 ± 0.03	−0.10 ± 0.03	−0.12 ± 0.04
6558150	Turn-off	2.52 ± 0.05	−0.03 ± 0.12	−0.02 ± 0.04	−0.12 ± 0.03	−0.15 ± 0.02	−0.08 ± 0.03	−0.07 ± 0.04
6568768	Turn-off	–	0.00 ± 0.12	−0.03 ± 0.04	−0.03 ± 0.03	−0.09 ± 0.03	−0.09 ± 0.03	−0.05 ± 0.05
6573727	Turn-off	2.47 ± 0.05	−0.09 ± 0.12	−0.11 ± 0.03	−0.14 ± 0.03	−0.09 ± 0.03	−0.07 ± 0.03	−0.08 ± 0.04
6573191	Turn-off	–	−0.02 ± 0.11	−0.01 ± 0.04	−0.11 ± 0.03	−0.11 ± 0.03	−0.10 ± 0.02	−0.06 ± 0.04
6572337	Turn-off	2.35 ± 0.05	−0.05 ± 0.12	−0.02 ± 0.04	−0.08 ± 0.04	0.05 ± 0.03	−0.05 ± 0.03	−0.03 ± 0.04
6569861	Turn-off	2.26 ± 0.05	−0.03 ± 0.11	−0.10 ± 0.04	−0.12 ± 0.03	−0.22 ± 0.03	−0.10 ± 0.03	−0.06 ± 0.04
6564445	Turn-off	2.22 ± 0.05	−0.16 ± 0.12	0.00 ± 0.04	0.00 ± 0.04	−0.17 ± 0.03	−0.03 ± 0.02	−0.06 ± 0.04
6567617	Turn-off	2.68 ± 0.05	−0.03 ± 0.12	−0.05 ± 0.04	−0.07 ± 0.04	−0.05 ± 0.03	−0.04 ± 0.03	−0.07 ± 0.04
6559497	Turn-off	2.58 ± 0.05	−0.06 ± 0.12	0.02 ± 0.04	−0.05 ± 0.04	−0.10 ± 0.02	−0.01 ± 0.02	0.00 ± 0.04
6568479	Turn-off	1.71 ± 0.05	−0.09 ± 0.12	−0.06 ± 0.04	−0.09 ± 0.03	−0.11 ± 0.02	−0.08 ± 0.03	−0.08 ± 0.04
6572560	Turn-off	2.51 ± 0.05	−0.06 ± 0.12	0.04 ± 0.03	−0.02 ± 0.03	−0.09 ± 0.03	−0.06 ± 0.03	−0.02 ± 0.04
6572187	Turn-off	2.06 ± 0.05	0.02 ± 0.12	0.00 ± 0.04	−0.05 ± 0.03	−0.07 ± 0.03	−0.04 ± 0.03	0.00 ± 0.04
6560653	Turn-off	2.43 ± 0.05	−0.11 ± 0.12	−0.08 ± 0.04	−0.12 ± 0.03	−0.06 ± 0.03	−0.10 ± 0.03	−0.06 ± 0.04
6567233	Turn-off	2.65 ± 0.05	0.02 ± 0.12	0.02 ± 0.04	−0.02 ± 0.03	−0.07 ± 0.02	−0.03 ± 0.03	−0.01 ± 0.05
6569167	Turn-off	2.45 ± 0.05	−0.05 ± 0.12	−0.06 ± 0.03	−0.04 ± 0.03	−0.15 ± 0.03	−0.04 ± 0.03	−0.02 ± 0.04
6565967	Turn-off	2.62 ± 0.05	−0.01 ± 0.12	0.02 ± 0.04	−0.06 ± 0.03	−0.03 ± 0.03	−0.03 ± 0.03	0.02 ± 0.04
6562672	Turn-off	2.42 ± 0.05	−0.05 ± 0.12	−0.17 ± 0.03	−0.15 ± 0.03	−0.14 ± 0.03	−0.17 ± 0.03	−0.13 ± 0.04
6571851	Turn-off	2.34 ± 0.05	−0.06 ± 0.11	−0.09 ± 0.04	−0.12 ± 0.03	−0.12 ± 0.03	−0.06 ± 0.03	−0.08 ± 0.04
6568307	Turn-off	–	−0.05 ± 0.12	0.01 ± 0.04	0.00 ± 0.04	−0.08 ± 0.03	−0.04 ± 0.03	−0.02 ± 0.04
8436138	Turn-off	2.34 ± 0.05	−0.06 ± 0.12	−0.08 ± 0.03	−0.11 ± 0.03	−0.12 ± 0.04	−0.08 ± 0.03	−0.05 ± 0.04
6571594	Turn-off	2.13 ± 0.05	−0.01 ± 0.12	−0.02 ± 0.03	−0.01 ± 0.03	0.04 ± 0.03	−0.03 ± 0.02	−0.01 ± 0.04
6579199	Turn-off	2.21 ± 0.05	−0.02 ± 0.12	−0.10 ± 0.03	−0.06 ± 0.03	−0.02 ± 0.03	−0.06 ± 0.03	0.03 ± 0.05
6562188	Turn-off	–	0.12 ± 0.11	−0.07 ± 0.04	−0.05 ± 0.03	−0.16 ± 0.02	−0.11 ± 0.03	−0.05 ± 0.05
6567847	Turn-off	–	−0.01 ± 0.12	0.01 ± 0.03	−0.08 ± 0.03	−0.10 ± 0.05	−0.04 ± 0.02	−0.02 ± 0.04
6563234	Turn-off	–	−0.01 ± 0.12	0.05 ± 0.04	0.05 ± 0.04	−0.06 ± 0.04	−0.03 ± 0.03	0.00 ± 0.04
9077970	Sub-giant	–	0.12 ± 0.13	0.02 ± 0.04	0.00 ± 0.03	−0.07 ± 0.02	0.03 ± 0.03	0.02 ± 0.04
6568921	Sub-giant	–	0.05 ± 0.12	0.01 ± 0.04	0.02 ± 0.03	−0.01 ± 0.02	0.00 ± 0.03	−0.02 ± 0.04
6574583	Sub-giant	–	−0.01 ± 0.13	0.08 ± 0.04	0.08 ± 0.03	0.10 ± 0.03	0.04 ± 0.03	0.07 ± 0.04
6562991	Sub-giant	–	0.00 ± 0.13	−0.04 ± 0.04	0.01 ± 0.04	−0.04 ± 0.03	0.00 ± 0.03	−0.01 ± 0.04
6569862	Sub-giant	–	0.01 ± 0.13	−0.04 ± 0.04	−0.05 ± 0.04	0.01 ± 0.03	0.03 ± 0.04	−0.02 ± 0.04
6567693	Sub-giant	–	0.12 ± 0.13	−0.14 ± 0.04	−0.08 ± 0.04	−0.09 ± 0.03	−0.10 ± 0.04	−0.12 ± 0.04
6577630	Sub-giant	–	−0.14 ± 0.13	−0.02 ± 0.05	−0.08 ± 0.04	−0.02 ± 0.02	−0.07 ± 0.04	−0.05 ± 0.04
6562765	Sub-giant	–	−0.15 ± 0.13	−0.06 ± 0.05	−0.02 ± 0.04	−0.02 ± 0.03	−0.04 ± 0.04	−0.05 ± 0.04
6569012	Sub-giant	–	−0.15 ± 0.14	0.06 ± 0.05	0.17 ± 0.04	0.10 ± 0.03	0.02 ± 0.05	0.07 ± 0.04
6571766	Red-giant	–	0.04 ± 0.14	−0.08 ± 0.04	0.01 ± 0.04	0.02 ± 0.02	−0.06 ± 0.05	−0.07 ± 0.05
6565104	Red-giant	–	−0.09 ± 0.14	−0.04 ± 0.04	0.00 ± 0.04	0.06 ± 0.03	0.01 ± 0.05	−0.03 ± 0.05
6579331	Red-giant	–	0.20 ± 0.14	−0.05 ± 0.06	−0.02 ± 0.04	0.02 ± 0.03	0.00 ± 0.04	−0.04 ± 0.04
6573364	Red-giant	–	−0.05 ± 0.14	−0.03 ± 0.05	−0.03 ± 0.04	−0.01 ± 0.03	−0.01 ± 0.04	−0.01 ± 0.05
6563655	Red-giant	–	−0.04 ± 0.15	0.02 ± 0.04	0.11 ± 0.04	0.18 ± 0.03	0.05 ± 0.05	0.03 ± 0.05
6570514	Red-giant	–	−0.08 ± 0.14	−0.05 ± 0.04	−0.11 ± 0.04	−0.02 ± 0.03	0.01 ± 0.05	−0.06 ± 0.04
6568851	Red-giant	–	0.00 ± 0.15	−0.09 ± 0.05	−0.12 ± 0.04	0.06 ± 0.03	−0.05 ± 0.05	−0.07 ± 0.05
6565879	Red-giant	–	0.07 ± 0.15	−0.09 ± 0.05	−0.15 ± 0.04	0.10 ± 0.03	−0.01 ± 0.05	−0.09 ± 0.04
6569711	Red-giant	–	0.00 ± 0.14	−0.05 ± 0.04	−0.19 ± 0.04	0.00 ± 0.04	−0.10 ± 0.05	−0.13 ± 0.05
6575356	Red-clump	–	−0.06 ± 0.14	0.04 ± 0.05	−0.12 ± 0.04	0.05 ± 0.03	−0.03 ± 0.05	−0.08 ± 0.05
6577481	Red-clump	–	−0.22 ± 0.15	0.05 ± 0.04	−0.09 ± 0.05	0.01 ± 0.03	−0.03 ± 0.05	−0.07 ± 0.05
6573728	Red-clump	–	−0.13 ± 0.15	0.05 ± 0.05	−0.08 ± 0.04	0.00 ± 0.04	−0.03 ± 0.04	−0.09 ± 0.05
6566179	Red-clump	–	0.12 ± 0.15	0.12 ± 0.05	−0.03 ± 0.05	0.06 ± 0.03	0.02 ± 0.05	−0.05 ± 0.05
6569393	Red-clump	–	0.07 ± 0.15	−0.07 ± 0.04	−0.14 ± 0.05	0.00 ± 0.03	−0.01 ± 0.05	−0.10 ± 0.05
6572270	Red-clump	–	0.00 ± 0.15	0.06 ± 0.05	−0.13 ± 0.04	0.03 ± 0.03	−0.01 ± 0.05	−0.08 ± 0.05

Table B2. LTE chemical abundances of the sample stars in M67. Abundances were derived relative to non-LTE values of solar analysed in this work.

GALAH ID	Group	A(Li)$_{\rm LTE}$	[O/H]$_{\rm LTE}$	[Na/H]$_{\rm LTE}$	[Mg/H]$_{\rm LTE}$	[Al/H]$_{\rm LTE}$	[Si/H]$_{\rm LTE}$	[Fe/H]$_{\rm LTE}$
6561552	Main-sequence	–	0.33 ± 0.10	0.07 ± 0.05	−0.03 ± 0.04	0.06 ± 0.02	0.00 ± 0.03	−0.02 ± 0.05
6560101	Turn-off	2.68 ± 0.05	0.32 ± 0.10	0.11 ± 0.04	−0.09 ± 0.03	−0.21 ± 0.02	−0.02 ± 0.03	−0.03 ± 0.04
6577714	Turn-off	2.66 ± 0.05	0.24 ± 0.10	0.07 ± 0.04	−0.14 ± 0.03	−0.02 ± 0.02	−0.04 ± 0.03	−0.05 ± 0.05
6554484	Turn-off	2.68 ± 0.05	0.22 ± 0.10	0.19 ± 0.04	−0.07 ± 0.03	−0.04 ± 0.02	−0.05 ± 0.03	0.05 ± 0.04
6577148	Turn-off	–	0.37 ± 0.10	0.16 ± 0.04	−0.13 ± 0.03	−0.14 ± 0.02	−0.04 ± 0.03	−0.03 ± 0.04
6569011	Turn-off	2.34 ± 0.05	0.37 ± 0.10	0.20 ± 0.04	−0.10 ± 0.03	−0.07 ± 0.02	−0.04 ± 0.03	0.00 ± 0.04
6565966	Turn-off	2.54 ± 0.05	0.22 ± 0.10	0.13 ± 0.04	−0.11 ± 0.03	−0.03 ± 0.03	−0.07 ± 0.03	−0.03 ± 0.04
6565326	Turn-off	2.42 ± 0.05	0.37 ± 0.10	0.23 ± 0.04	−0.10 ± 0.03	−0.02 ± 0.02	−0.02 ± 0.03	0.03 ± 0.04
6574584	Turn-off	–	0.29 ± 0.11	0.16 ± 0.04	−0.06 ± 0.03	−0.11 ± 0.02	−0.06 ± 0.03	0.00 ± 0.04
6571679	Turn-off	–	0.38 ± 0.10	0.19 ± 0.03	−0.10 ± 0.03	−0.17 ± 0.02	−0.06 ± 0.03	−0.04 ± 0.04
6567547	Turn-off	2.52 ± 0.05	0.26 ± 0.10	0.16 ± 0.04	−0.10 ± 0.03	−0.05 ± 0.02	0.00 ± 0.02	0.04 ± 0.04
6555602	Turn-off	–	0.32 ± 0.10	0.11 ± 0.04	−0.18 ± 0.03	−0.13 ± 0.02	−0.10 ± 0.03	−0.07 ± 0.04
6561039	Turn-off	2.70 ± 0.05	0.39 ± 0.10	0.07 ± 0.04	−0.06 ± 0.03	−0.11 ± 0.02	−0.02 ± 0.03	−0.05 ± 0.05
6570179	Turn-off	2.44 ± 0.05	0.28 ± 0.10	0.04 ± 0.04	−0.18 ± 0.03	−0.23 ± 0.03	−0.13 ± 0.03	−0.14 ± 0.04
6564123	Turn-off	2.38 ± 0.05	0.26 ± 0.10	0.11 ± 0.04	−0.05 ± 0.03	−0.11 ± 0.02	−0.06 ± 0.02	0.00 ± 0.05
6573044	Turn-off	2.45 ± 0.05	0.24 ± 0.10	0.13 ± 0.04	−0.12 ± 0.03	−0.13 ± 0.03	−0.04 ± 0.03	−0.03 ± 0.04
6575508	Turn-off	2.23 ± 0.05	0.29 ± 0.10	0.03 ± 0.04	−0.16 ± 0.03	−0.21 ± 0.02	−0.08 ± 0.03	−0.11 ± 0.05
6558150	Turn-off	2.52 ± 0.05	0.30 ± 0.10	0.17 ± 0.04	−0.15 ± 0.03	−0.14 ± 0.02	−0.07 ± 0.03	−0.06 ± 0.05
6568768	Turn-off	–	0.39 ± 0.10	0.14 ± 0.04	−0.07 ± 0.03	−0.09 ± 0.03	−0.08 ± 0.03	−0.04 ± 0.04
6573727	Turn-off	2.47 ± 0.05	0.18 ± 0.10	0.05 ± 0.04	−0.17 ± 0.03	−0.08 ± 0.02	−0.06 ± 0.03	−0.07 ± 0.04
6573191	Turn-off	–	0.35 ± 0.10	0.18 ± 0.04	−0.14 ± 0.04	−0.10 ± 0.02	−0.09 ± 0.02	−0.05 ± 0.05
6572337	Turn-off	2.35 ± 0.05	0.21 ± 0.11	0.16 ± 0.04	−0.10 ± 0.03	0.06 ± 0.03	−0.04 ± 0.03	−0.01 ± 0.04
6569861	Turn-off	2.26 ± 0.05	0.24 ± 0.10	0.06 ± 0.04	−0.15 ± 0.03	−0.21 ± 0.02	−0.09 ± 0.02	−0.05 ± 0.04
6564445	Turn-off	2.22 ± 0.05	0.13 ± 0.10	0.19 ± 0.04	−0.03 ± 0.03	−0.16 ± 0.03	−0.02 ± 0.02	−0.05 ± 0.04
6567617	Turn-off	2.68 ± 0.05	0.27 ± 0.11	0.14 ± 0.04	−0.10 ± 0.03	−0.04 ± 0.03	−0.02 ± 0.03	−0.06 ± 0.05
6559497	Turn-off	2.58 ± 0.05	0.24 ± 0.10	0.20 ± 0.04	−0.08 ± 0.03	−0.08 ± 0.02	0.00 ± 0.03	0.01 ± 0.05
6568479	Turn-off	1.71 ± 0.05	0.17 ± 0.11	0.07 ± 0.04	−0.12 ± 0.03	−0.10 ± 0.03	−0.07 ± 0.03	−0.07 ± 0.04
6572560	Turn-off	2.50 ± 0.05	0.36 ± 0.11	0.23 ± 0.04	−0.07 ± 0.03	−0.08 ± 0.03	−0.04 ± 0.03	0.00 ± 0.04
6572187	Turn-off	2.05 ± 0.05	0.30 ± 0.10	0.18 ± 0.04	−0.07 ± 0.03	−0.05 ± 0.03	−0.02 ± 0.03	0.01 ± 0.05
6560653	Turn-off	2.43 ± 0.05	0.13 ± 0.10	0.09 ± 0.04	−0.14 ± 0.03	−0.04 ± 0.02	−0.09 ± 0.03	−0.05 ± 0.05
6567233	Turn-off	2.65 ± 0.05	0.28 ± 0.10	0.19 ± 0.05	−0.04 ± 0.03	−0.05 ± 0.02	−0.02 ± 0.03	0.00 ± 0.04
6569167	Turn-off	2.45 ± 0.05	0.28 ± 0.11	0.12 ± 0.04	−0.08 ± 0.03	−0.14 ± 0.03	−0.02 ± 0.03	0.00 ± 0.04
6565967	Turn-off	2.62 ± 0.05	0.28 ± 0.11	0.20 ± 0.04	−0.08 ± 0.03	−0.01 ± 0.02	−0.02 ± 0.02	0.03 ± 0.04
6562672	Turn-off	2.42 ± 0.05	0.20 ± 0.10	−0.01 ± 0.04	−0.17 ± 0.03	−0.13 ± 0.03	−0.16 ± 0.02	−0.12 ± 0.05
6571851	Turn-off	2.34 ± 0.05	0.17 ± 0.10	0.08 ± 0.04	−0.14 ± 0.03	−0.11 ± 0.02	−0.04 ± 0.03	−0.06 ± 0.05
6568307	Turn-off	–	0.32 ± 0.11	0.21 ± 0.04	−0.06 ± 0.03	−0.07 ± 0.02	−0.03 ± 0.03	0.01 ± 0.04
8436138	Turn-off	2.34 ± 0.05	0.18 ± 0.10	0.10 ± 0.04	−0.12 ± 0.04	−0.10 ± 0.03	−0.06 ± 0.02	−0.04 ± 0.05
6571594	Turn-off	2.12 ± 0.05	0.37 ± 0.10	0.18 ± 0.04	−0.05 ± 0.03	0.06 ± 0.02	−0.01 ± 0.02	0.02 ± 0.05
6579199	Turn-off	2.21 ± 0.05	0.23 ± 0.10	0.06 ± 0.04	−0.09 ± 0.03	0.00 ± 0.03	−0.05 ± 0.03	0.04 ± 0.04
6562188	Turn-off	–	0.40 ± 0.10	0.10 ± 0.04	−0.07 ± 0.03	−0.14 ± 0.02	−0.09 ± 0.02	−0.04 ± 0.05
6567847	Turn-off	–	0.35 ± 0.11	0.20 ± 0.04	−0.12 ± 0.04	−0.07 ± 0.04	−0.03 ± 0.03	0.00 ± 0.04
6563234	Turn-off	–	0.35 ± 0.11	0.26 ± 0.04	0.00 ± 0.03	−0.04 ± 0.03	−0.01 ± 0.03	0.03 ± 0.04
9077970	Sub-giant	–	0.36 ± 0.12	0.21 ± 0.04	−0.02 ± 0.03	−0.02 ± 0.02	0.05 ± 0.03	0.05 ± 0.04
6568921	Sub-giant	–	0.29 ± 0.12	0.20 ± 0.04	0.00 ± 0.03	0.03 ± 0.02	0.01 ± 0.03	0.01 ± 0.05
6574583	Sub-giant	–	0.17 ± 0.12	0.25 ± 0.05	0.07 ± 0.03	0.15 ± 0.03	0.06 ± 0.03	0.11 ± 0.05
6562991	Sub-giant	–	0.17 ± 0.12	0.13 ± 0.05	0.00 ± 0.04	0.01 ± 0.03	0.02 ± 0.03	0.02 ± 0.05
6569862	Sub-giant	–	0.16 ± 0.13	0.13 ± 0.05	−0.05 ± 0.03	0.06 ± 0.02	0.05 ± 0.03	0.01 ± 0.05
6567693	Sub-giant	–	0.29 ± 0.12	0.03 ± 0.05	−0.07 ± 0.03	−0.03 ± 0.03	−0.09 ± 0.04	−0.09 ± 0.05
6577630	Sub-giant	–	−0.02 ± 0.13	0.14 ± 0.05	−0.07 ± 0.03	0.04 ± 0.03	−0.06 ± 0.04	−0.02 ± 0.05
6562765	Sub-giant	–	−0.03 ± 0.13	0.10 ± 0.05	−0.01 ± 0.03	0.05 ± 0.03	−0.02 ± 0.04	−0.02 ± 0.04
6569012	Sub-giant	–	−0.03 ± 0.13	0.24 ± 0.05	0.18 ± 0.03	0.16 ± 0.03	0.04 ± 0.04	0.10 ± 0.05
6571766	Red-giant	–	0.17 ± 0.13	0.08 ± 0.07	0.03 ± 0.04	0.09 ± 0.03	−0.04 ± 0.04	−0.03 ± 0.05
6565104	Red-giant	–	0.04 ± 0.13	0.14 ± 0.06	0.02 ± 0.04	0.14 ± 0.03	0.03 ± 0.05	0.04 ± 0.05
6579331	Red-giant	–	0.37 ± 0.13	0.14 ± 0.06	0.00 ± 0.04	0.10 ± 0.03	0.02 ± 0.05	0.01 ± 0.05
6573364	Red-giant	–	0.09 ± 0.13	0.18 ± 0.06	−0.02 ± 0.04	0.07 ± 0.03	0.01 ± 0.04	0.05 ± 0.06
6563655	Red-giant	–	0.10 ± 0.14	0.23 ± 0.05	0.12 ± 0.04	0.27 ± 0.03	0.07 ± 0.04	0.09 ± 0.05
6570514	Red-giant	–	0.05 ± 0.14	0.15 ± 0.05	−0.09 ± 0.04	0.05 ± 0.04	0.04 ± 0.04	−0.01 ± 0.05
6568851	Red-giant	–	0.15 ± 0.14	0.13 ± 0.06	−0.11 ± 0.04	0.15 ± 0.03	−0.02 ± 0.05	−0.02 ± 0.05
6565879	Red-giant	–	0.21 ± 0.14	0.15 ± 0.06	−0.13 ± 0.04	0.19 ± 0.03	0.01 ± 0.05	−0.02 ± 0.04
6569711	Red-giant	–	0.14 ± 0.14	0.18 ± 0.06	−0.17 ± 0.04	0.10 ± 0.04	−0.07 ± 0.05	−0.06 ± 0.05
6575356	Red-clump	–	0.13 ± 0.15	0.28 ± 0.05	−0.12 ± 0.04	0.15 ± 0.03	0.01 ± 0.05	0.00 ± 0.05
6577481	Red-clump	–	−0.07 ± 0.15	0.29 ± 0.05	−0.10 ± 0.04	0.12 ± 0.03	0.01 ± 0.04	0.01 ± 0.05
6573728	Red-clump	–	0.05 ± 0.14	0.28 ± 0.05	−0.07 ± 0.03	0.10 ± 0.03	0.00 ± 0.05	−0.01 ± 0.05
6566179	Red-clump	–	0.29 ± 0.14	0.34 ± 0.05	−0.03 ± 0.04	0.18 ± 0.03	0.05 ± 0.05	0.04 ± 0.05
6569393	Red-clump	–	0.25 ± 0.15	0.16 ± 0.05	−0.13 ± 0.04	0.10 ± 0.03	0.03 ± 0.05	−0.04 ± 0.05
6573270	Red-clump	–	0.16 ± 0.15	0.28 ± 0.05	−0.12 ± 0.04	0.15 ± 0.04	0.03 ± 0.05	0.00 ± 0.05